Research Square

Preprints are preliminary reports that have not undergone peer review.
They should not be considered conclusive, used to inform clinical practice,
or referenced by the media as validated information.

Holographic measurement of discrete bubbles in cavitating flow and optimization of a multiscale Eulerian-Lagrangian model

Yuntian Wang

nowheeldrive@163.com

Beijing Institute of Technology Zhuhai: Beijing Institute of Technology - Zhuhai Campus
https://orcid.org/0009-0001-6479-0203

Beichen Tian

Beijing Institute of Technology Zhuhai: Beijing Institute of Technology - Zhuhai Campus

Weiye Zhong

Zhejiang Sci-Tech University

Linmin Li

Zhejiang Sci-Tech University

Biao Huang

Beijing Institute of Technology Zhuhai: Beijing Institute of Technology - Zhuhai Campus

Research Article

Keywords: Digital in-line holography, cavitating flow, multiscale, Eulerian-Lagrangian model

Posted Date: March 30th, 2026

DOI: https://doi.org/10.21203/rs.3.rs-9177352/v1

License: This work is licensed under a Creative Commons Attribution 4.0 International License.
Read Full License

Holographic measurement of discrete bubbles in cavitating flow and optimization of a multiscale Eulerian-Lagrangian model

Yuntian Wang [1], Beichen Tian [1,2,*], Weiye Zhong [3], Linmin Li [3], Biao Huang [1,2,*]

[1] Energy and Transportation Domain, Beijing Institute of Technology, Zhuhai 519088, China

[2] School of Mechanical Engineering, Beijing Institute of Technology, Beijing 100081, China

[3] Key Laboratory of Fluid Transmission Technology of Zhejiang Province, Zhejiang SciTech University, Hangzhou 310018, China

Abstract: This study integrates experimental measurements and numerical simulations to systematically investigate multiscale cavitation bubble dynamics in cloud cavitating flow around a NACA66 hydrofoil. Full flow field high-speed imaging technology conducted under an inflow velocity of 8.5 m/s and a cavitation number of 1.4 shows that macroscopic cavity structures display typical periodic evolutionary behavior, including three evolution stages of growth of attached cavity, development of re-entrant jet and cloud cavity shedding. The observed shedding frequency is approximately 45.55 Hz, and the maximum attached cavity length reaches 0.8 times the chord length of hydrofoil. Quantitative measurements of cavitation nuclei in the incoming flow and discrete microbubbles within the cavitation zone are acquired via digital in-line holography (DIH) technology. In the inflow region, the number density and average size of cavitation nuclei exhibit minor temporal fluctuations. In contrast, the spatial number density of microbubbles in the cavity shedding region and the wake flow region shows periodic evolution in response to the development of cloud cavitation. Meanwhile, the bubble size distribution follows a dual-power-law pattern, with smaller bubbles adhering to a −4/3 power-law scaling and larger ones conforming to a −10/3 scaling. Additionally, a Eulerian–Lagrangian two-way coupled model is optimized based on the experimental holographic imaging data of microbubble in cloud cavitating flow. Large Eddy Simulation (LES) coupled with the Volume of Fluid (VOF) method is employed for macroscopic cavity dynamics in the Eulerian framework, while the dynamics of nuclei and microbubbles are addressed via a Discrete Bubble Model (DBM) in the Lagrangian framework. The model incorporates physically-based conversion criteria to couple the two frameworks and is validated against experimental observations of microbubble behavior. Validation results demonstrate that the improved model accurately predicts cavitation shedding frequency, cavity morphology, and bubble number density distribution, confirming its reliability and predictive capability for simulating multiscale cavitation dynamics.

Key words: Digital in-line holography, cavitating flow, multiscale, Eulerian-Lagrangian model

0. Introduction

Cloud cavitation is an extremely complex and multiphase physical hydrodynamic phenomenon in hydraulic machinery such as turbines, propellers, and pumps under high-speed and high-load operating conditions [1–3]. Under the influence of complex turbulent structures, the cloud cavitating flow field exhibits complex multiscale behavior, with the length scale of vapor structures spanning micrometer to meter scales [4–6]. The cavitation loads resulting from macroscale cavity oscillation, rupture, and microbubble collapse can lead to structural vibrations, material erosion, and radiated noise [7–10]. Currently, the lack of quantitative data on mesoscopic bubble clusters during the evolution of cloud cavitating flow significantly restricts the accurate prediction of cavity dynamics and load characteristics. Therefore, developing refined measurement and simulation methods for cavitating flow represents a

[P]roject supported by the Beijing Natural Science Foundation (JQ25012), and the National Natural Science Foundation of China (Grant Nos: 52441903, 92582103 and U22B6010)

Biography: Yuntian Wang (2003-), Male, Ph. D. Candidate, E-mail: Nowheeldrive@163.com

Corresponding author: Beichen Tian, E-mail: 18810578969@163.com; Biao Huang, E-mail: huangbiao@bit.edu.cn

critical scientific challenge in cavitation research.

Over recent decades, high-speed visualization techniques have been developed to investigate unsteady dynamics in cloud cavitating flows, typically employing simple geometries such as hydrofoils, convergent-divergent channels and axisymmetric bodies in water tunnel experiments [11–14]. With the decrease of cavitation number, cavitating flow gradually develops into inception cavitation, sheet cavitation, cloud cavitation and super cavitation [15–17]. Among these cavitation regimes, inception, sheet, and super cavitation flows exhibit relatively stable structures. The inception cavitation typically manifests as clusters of microscopic bubbles, which form when the local pressure in the fluid falls below the saturated vapor pressure, causing cavitation nuclei to expand into visible bubbles[18]. As the local pressure decreases further, these bubbles develop into a relatively stable thin vapor film attached to a solid surface, with its trailing edge often subject to small-amplitude shedding, which is defined as sheet cavitation[19]. Super cavitation develops as the cavity grows sufficiently to completely envelop the body in the flow, forming a continuous vapor layer[20]. Up to now, each of these cavitation stages still presents unresolved scientific challenges. For instance, predicting nuclei dynamics during inception is highly complex, as models are sensitive to the initial size and distribution of nuclei, which can easily introduce errors[21]. Furthermore, the pressure threshold is subject to considerable uncertainty because the inception cavitation index is significantly influenced by local pressure fluctuations and water quality. While the stability of super cavity is governed by closure mechanisms include re-entrant jet, twin-vortex, or four-vortex closure modes, which are susceptible to flow disturbances and gravitational effects, thereby constituting a distinct set of research challenges[22]. In contrast, cloud cavitation is regarded as one of the most challenging and significant types owing to its wide operational condition range, intricate flow structures, and highly unsteady load fluctuations. This phenomenon typically occurs when a largescale attached cavity undergoes periodic pinch-off and shedding downstream, driven by mechanisms such as re-entrant jets [23,24], condensation shockwaves [25,26], or Kelvin–Helmholtz instabilities [27]. Under the comprehensive effects of the main flow and complex vortices, the detached sheet cavity evolves into various scale vapor structures [28]. Additionally, compared to other cavitation stages, cloud cavitation, characterized by more pronounced multiscale effects, has emerged as a highly challenging research subject. The collapse of numerous bubbles within the cloud cavitation flow field is more likely to induce complex hydrodynamic load, such as structural vibrations, material erosion, and radiated noise [7–10] holding significant scientific and engineering research value. However, the currently available data on discrete bubble scales and vapor content distribution within shedding cavities are extremely limited, resulting in a significant gap between the mechanical models and numerical simulation methods for unsteady characteristics, cavitation erosion, and noise in cavitating flows. Under the influence of turbulent structures, large cavities break up into smaller vapor structures[29], and the high-frequency pressure pulses generated by the collapse of microbubbles can induce significant hydraulic loads[30]. To predict such phenomena, researchers have established quantitative relationships between bubble dynamics and cavitation loads based on the distribution characteristics of discrete bubble clusters. By combining an ideal acoustic spectral function for single-bubble collapse with empirical bubble population parameters, Yamada et al.[31] achieved quantitative prediction of tip vortex cavitation noise, with errors within 3 dB in the high-frequency range compared to measured data. Wang et al.[32] coupled discrete bubble dynamics with the permeable acoustic analogy method. Leveraging the high natural frequency and multiple collapse-rebound behavior of microbubbles during cavitation collapse, along with bubble cluster distributions resulting from cavity fission and environmental nucleation, they significantly improved the accuracy of high-frequency noise prediction. In another study, Wang et al.[33]

developed a two-way coupled Euler–Lagrange multi-scale cavitation erosion model. Based on numerically obtained bubble size parameters following a Gaussian distribution, they quantified the impact pressure and erosion intensity generated by bubble oscillations, enabling quantitative assessment of erosion caused by microscale bubble clusters, with predicted pressures reaching up to 10^7 Pa. These studies consistently demonstrate that data on the number and size distribution of discrete bubble clusters form a critical link connecting microscopic bubble dynamics with the prediction of macroscopic high-frequency cavitation noise and loads. Therefore, achieving quantitative experimental measurement of bubble clusters is of great significance for further research in the field of cavitation.

In view of the significant importance of quantitative information of discrete microbubbles, extensive research efforts have been devoted to measuring cavitating flow fields, especially to characterize the discrete bubbles in shedding cloud cavities, using a variety of techniques. Due to its structural simplicity and exceptional stability, the probe-based measurement technique is widely employed to record the time-history of vapor signals within cavitation zones [34]. Subsequent analysis of signal amplitude provides statistical characterization of bubble size distributions. Stutz et al. [35] utilized an optical probe to investigate the average void fraction, bubble velocity, and bubble size distribution in the bubbly flow. Zhang et al. used a fiber-optic phase detection probe to measure mixture information inside sheet/cloud cavities in cavitating flow around a NACA0012 hydrofoil. Measurements of small-scale vapor structure characteristics were conducted along the vertical direction at 1 mm intervals on the hydrofoil midspan, specifically at a location one-third chord length upstream from the trailing edge and at the trailing edge of hydrofoil. The results indicated that the probability density function of the bubble number as a function of bubble size followed a lognormal distribution, with the peak occurring at a bubble diameter of approximately 0.5 mm[36]. Furthermore, Liu *et al.*[37] utilized optical fiber probe measurements to characterize discrete bubble dynamics within the cavitating flow field surrounding a hydrofoil, revealing a dual power-law scaling law of microbubble size distribution, with exponents of -10/3 and -4/3, during the development of cloud cavitation. However, the intrusive nature of the probe introduces measurement bias by piercing cavitation bubbles and causing hydrodynamic interference, which is particularly pronounced when measuring mesoscale bubbles. In contrast, compared with other non-invasive optical measurement techniques, digital in-line holography (DIH) is particularly distinguished for the application in the characterization of discrete bubbles within multiphase flows, owing to its cost-effectiveness, minimal experimental setup, and superior spatial resolution. Traditional optical holography originated in the 1940s [38], can capture the complete optical field information of multiphase flow fields by leveraging the principles of light diffraction and interference, thereby enabling the acquisition of three-dimensional size, spatial position, and velocity information of discrete particles [39]. Lebrun *et al.* [40] employed DIH method to investigate the size distribution and concentration of microscale nuclei in a cavitation tunnel under varying ambient pressures. Their results identified a nuclei population with diameters ranging from 6 μm to 100 μm, which decreased in abundance with increasing size. Additionally, Kato et al. [41] also employed DIH technology to investigate the characteristics of microbubble size distribution inside cavitation region. These measurements reveal that the sizes of the discrete bubbles are primarily distributed within 300 micrometers and closely follow a power-law distribution. It is noteworthy that although DIH provides significant advantages for detecting discrete microbubbles in cavitating flows, the lack of systematic and quantitative measurements of microbubble populations inside cloud cavitating flow doubt on the accuracy of existing multiscale numerical models for cloud cavitation in simulating the discrete phase. Quantitative information on discrete cavitation bubbles is crucial for developing multiscale cavitation models, as their widespread presence is closely linked to the occurrence of

cavitation phenomena. Khoo et al.[42] systematically measured the concentration and diameter of cavitation nuclei in water under various operating conditions, and their data have since served as key parametric input for numerous multiscale cavitation simulation studies. However, there remains a lack of synchronized measurement data on incoming cavitation nuclei content under cloud cavitation conditions, making it difficult to establish accurate multiscale models for cloud cavitation. Furthermore, in the absence of quantitative measurement data for cavitation nuclei, conventional simulations typically rely on single-bubble expansion theory, which fails to capture the distribution characteristics of bubble clusters and cannot accurately describe how cavitation shedding mechanisms are modulated by bubble population evolution[43]. Moreover, due to the lack of quantitative validation data for discrete bubbles, existing numerical studies often compare results only with macroscopic observations, such as overall cavity morphology, shedding frequency, and pressure distribution on hydrofoil surfaces[5,44], which does not allow for a comprehensive validation of multiscale simulation performance. Therefore, it is crucial for cavitation research to systematically measure the size and distribution of discrete bubbles at different locations within the flow field under the same cavitation conditions.

The development of high-fidelity prediction for studying cavitation surge has also garnered significant attention in recent years, driven largely by progress in computational fluid dynamics [45]. In current researches, the homogeneous assumption is widely adopted to represent the two-phase system as a variable-density continuum in Euler framework. The interphase mass transfer is modeled using cavitation models such as Schnerr-Sauer (S-S) [46], Zwart-Gerber-Belamri (ZGB) [47], and Singhal [48], while the dynamic evolution of cavity structures is captured by interface capture methods, such as volume of fluid (VOF) [49] and level set (LS) [50]. However, conventional Eulerian methods are constrained by grid resolution and are consequently incapable of adequately resolving the multiscale features of cavitating flows. To address this limitation, multiscale cavitation models based on a Euler-Lagrange (E-L) framework have been developed to capture sub-grid microbubble dynamics[33,43,51–53]. Giannadakis *et al.* [54] were among the first to systematically account for the stochastic and multiscale nature of cavitation, proposing and validating a multiscale cavitation model based on a Eulerian–Lagrangian framework for simulating cavitation phenomena inside diesel nozzles. This model treats cavitation as the motion and evolution of discrete bubble clusters within a continuous liquid phase: when the local pressure falls below the vapor pressure, vapor bubbles are generated based on a predefined nuclei size distribution to determine number density, and bubbles with identical properties and no interaction are grouped into parcels, with bubble attributes generated stochastically via Monte Carlo methods. Additionally, the model incorporates several sub-models to describe the growth, motion, breakup, coalescence of discrete vapor bubbles, and their interaction with turbulence. When the volume of a discrete vapor bubble exceeds that of a grid cell, it transitions to a Eulerian method to resolve large-scale vapor structures. Chahine *et al.* [55] further investigated the growth and motion mechanisms of cavitation nuclei in non-uniform flow fields, proposing the Surface-Averaged Pressure (SAP) model as an improvement over traditional spherical bubble model. Combined with experimental data on cavitation nuclei, they developed a discrete bubble tracking model that accounts for nucleation effects. This model was eventually coupled with a viscous compressible flow solver to simulate two-phase flow under bubble injection propulsion conditions, and further evolved into a two-way coupled multiscale two-phase flow model. Ma *et al.* [56] focused on the influence of wall nucleation effects on cavitation simulation, establishing a Lagrangian Discrete Singularity Model (DSM) suitable for micron-sized bubbles, which was coupled with a Eulerian Level Set Method (LSM) for capturing large cavities, forming a bidirectional cross-scale numerical simulation method for cavitating flows. In this approach, micro-bubbles tracked

by DSM are converted into free surfaces resolved by LSM once they grow beyond a threshold based on the local grid; conversely, upon collapse of large cavities, they are decomposed into multiple micro-bubbles according to empirical criteria and handled by DSM. The authors validated the model through several typical cases, including bubble capture in a line vortex, cavitation over a NACA0015 hydrofoil, cavitation behind a blunt body, and propeller cavitation. Similarly, based on stochastic nucleation assumptions, Li *et al.* [57], Wang *et al.*[58], and Tian *et al.* [59] developed a discrete bubble model that considers the influence of cavitation nuclei in the flow domain. By tracking the motion and dynamic behavior of individual bubbles, they conducted numerical studies on the characteristics of cavitation micro-bubbles in simple geometries such as flow around hydrofoils and converging-diverging channels. When the size or sphericity of a discrete bubble exceeds a set threshold, or when it approaches a large-scale attached cavity, the model transitions it to the Eulerian framework for subsequent computation. Ghahramani *et al.* [6] and Wang *et al.*[33] argued that discrete bubbles primarily originate from the shedding and breakup of large-scale cavities. They proposed that when the size of an Eulerian cavity is smaller than the local grid size, it should be converted into spherical bubbles of equivalent volume and solved in the Lagrangian framework using the Rayleigh–Plesset (R–P) equation until the bubbles collapse in high-pressure regions or regrow beyond a critical grid size in low-pressure regions, at which point they transition back to the Eulerian framework, where the Volume of Fluid (VOF) method is used to capture large-scale cavity interfaces. Although multiscale cavitation simulation has been extensively studied, several issues remain to be addressed. Existing research has shown that the number, content, and size distribution of cavitation nuclei are key factors influencing the evolution behavior of multiscale bubbles in cavitating flows and the accuracy of Eulerian–Lagrangian simulations, a viewpoint further supported by studies from Zhang *et al.* [60]. However, the construction of most current multiscale cavitation models relies on historical experimental data. Direct application of these data under varying actual conditions or model configurations may lead to significant errors. In addition, the transition strategy between Eulerian and Lagrangian frameworks significantly impacts multiscale cavitation simulations, particularly the spatiotemporal evolution of discrete bubbles. Most current studies achieve framework transition by comparing discrete bubble size with artificially set Eulerian grid scales, an approach that remains highly controversial in terms of simulation accuracy. To enhance the reliability of Eulerian–Lagrangian simulations in the context of multiscale cavitating flows, further in-depth and systematic investigation of the aspects remains essential.

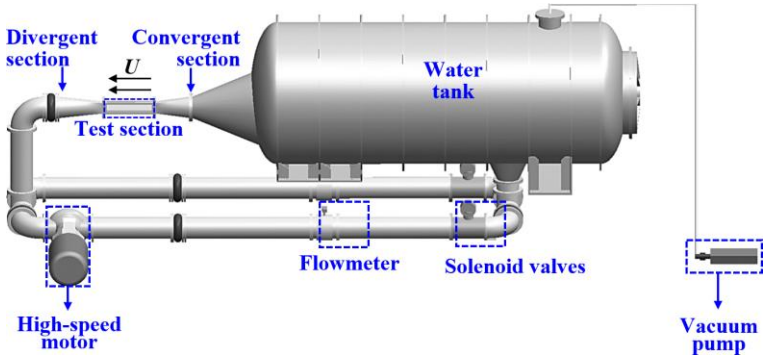
This study aims to systematically elucidate multiscale bubble dynamics in cloud cavitating flow around a NACA66 hydrofoil and to develop a high-fidelity prediction method through integrated advanced optical diagnostics and multiscale numerical simulations with experimental validation. The specific objectives are: (1) To integrate high-speed imaging and digital in-line holography (DIH) for quantitative characterization of the spatiotemporal evolution and size distribution of discrete microbubbles in the inflow, cavity shedding, and wake flow regions, thereby addressing the current lack of systematic quantitative data on bubble populations in cloud cavitation; (2) To optimize the cavitation nuclei initialization parameters and framework transition criteria in the Eulerian-Lagrangian multiscale cavitation model, based on holography-derived quantitative data, including microbubble number density, size distribution, and time-averaged Sauter mean diameter, thus reducing empirical dependence and enhancing the model's physical consistency and numerical robustness in simulating complex cavitating flows; (3) To validate the capability of the developed model in capturing transient multiscale cavitation evolution, through comprehensive experimental-numerical comparisons of macroscopic cavity morphology, shedding frequency, and microscopic bubble number density distributions, thereby

providing a reliable tool for cavitation dynamics prediction.

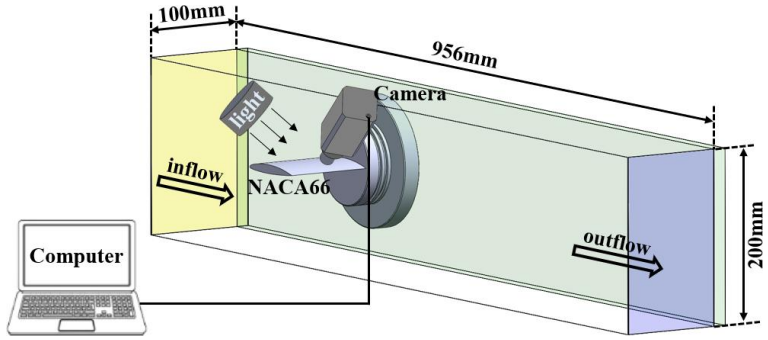
1. Experimental setup

1.1 *Experimental facility and global cavity observation system*

The experimental observation of cavity dynamics is carried out in a closed-loop cavitation water tunnel at the Beijing Institute of Technology, as illustrated in Fig. 1(a). The closed-loop cavitation water tunnel, with overall dimensions of 11.86 m in length and 4.9 m in height, consists of a water storage tank, convergent section with the shrinkage ratio of approximately 52:1, test section, divergent section, centrifugal pump, recirculating pipeline with expansion joints, and a vacuum pump. The water storage tank, with a capacity of 50 m^3, features a free surface for air separation and is connected to a vacuum pump that regulates pressure above the free surface from 0.01 to 0.2 MPa with an accuracy of ±0.005 MPa. Tap water is pre-treated by extended settling in a ground-level reservoir to remove dissolved gases and impurities, followed by an additional 24-hour settling period in a storage tank to stabilize air content and cavitation nuclei distribution. The entire water tunnel is driven by a centrifugal pump, while an electromagnetic flow meter monitors flow velocity with high precision. The flow velocity in the test section is adjustable up to 12 m/s, with a control accuracy of ±0.075 m/s, achieved through motor frequency regulation. Meanwhile, a honeycomb flow straightener mounted between the storage tank outlet and the convergent section reduces inflow turbulence and improves velocity uniformity entering the test section. Additionally, as shown in Fig. 1(b), the rectangular test section is 956 mm in length, 100 mm in width, and 200 mm in height. The NACA66 hydrofoil with a chord length (c) of 85 mm and a span (b) of 100 mm is positioned 239 mm downstream from the inlet plane of the test section at an angle of attack of 8 degrees. The cavitation structures on the hydrofoil suction surface are observed in an oblique view using a high-speed camera at 4000 fps, with illumination provided by a dedicated light source. The cavitation number $\sigma = 2(p_{ref} - p_v)/\rho U^2$, where p_{ref} is the tunnel pressure measured at the test section outlet, p_v is the saturated vapor pressure, and ρ is the fluid density.



(a) closed-loop cavitation water tunnel



(b) schematic of macroscale cavity acquisition system

Fig. 1. The schematic of measurement and acquisition system.

1.2 *Digital in-line holographic measurement system of microbubble*

To further characterize the bubbles within the flow field during cloud cavitation evolution, digital in-line holography (DIH) is employed to measure the size and spatial distribution of discrete microbubbles in present work. Fig. 2 depicts the schematic diagram of the experimental setup for mesoscale bubble holography and the corresponding measurement location. As shown in Fig. 2(a), a low-power laser pointer with a power output of 0.22 W served as the coherent light source, emitting a green laser beam at a wavelength of 532 nm with good coherence but low energy density. The laser beam is first expanded by a concave lens and then passes through two confocal convex lenses with focal lengths of 50 mm and 200 mm, respectively, resulting in a collimated beam with a diameter of 40 mm. Subsequently, the collimated laser beam is directed perpendicularly into the test section through the transparent observation windows. Meanwhile, on the opposite side of the test section, a high-speed camera equipped with a 105 mm lens and a neutral density (ND) filter is aligned coaxially with the laser beam to record holographic images. The pixel size of the high-speed camera is about 25.3 μm, and the pixel resolution is 1152 × 1080 pixels. The total of five repetitive measurements is performed, each including 1000 pictures consecutively recorded at a frame rate of 4000 fps. In addition, the high-resolution holographic measurements are performed at three different position to quantify both nuclei carried by inflow and discrete bubbles within cavitation zones. As shown in Fig. (2), the first position, A, is in the inflow region upstream of the hydrofoil at a position two-thirds of the chord length from the leading edge. The second position, B, is in the cavity shedding region directly above the hydrofoil, also at two-thirds of the chord length. The third position, C, is in the wake region downstream of the hydrofoil at a position four-thirds of the chord length from the leading edge. As schematically illustrated in Fig. 2(c), according to the fundamental principles of optical diffraction and interference, discrete microbubbles passing through the parallel laser beam in the test section induce diffraction, resulting in light deflection to form the object beam. The portion of the laser beam unaffected by the microbubbles and propagating uniformly through the fluid medium constitutes the reference beam. Along the propagation path, the object beam behind each microbubble interferes with the reference beam, generating alternating bright and dark interference fringes. This interference pattern, captured by a high-speed camera, forms a hologram encoding information about the size and depth coordinates of the individual microbubble.

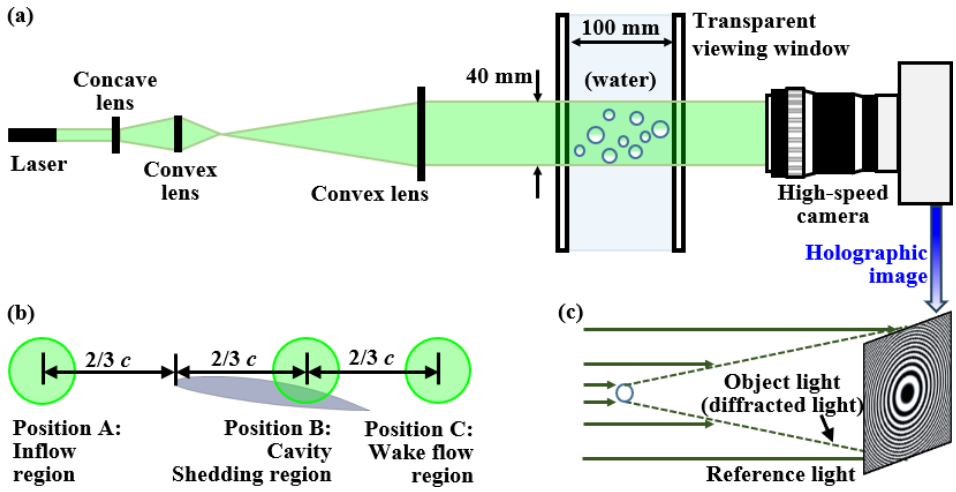
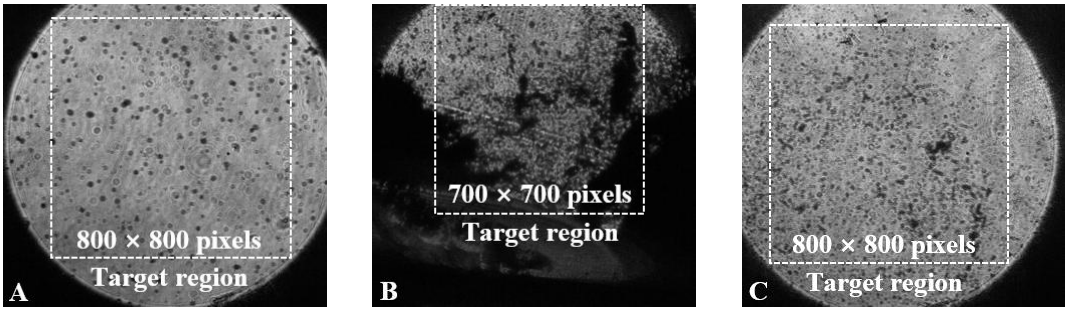


Fig.2. Schematic of DIH system. (a) Schematic diagram of microbubble measurement system based on holographic technology, (b) the relative position of the parallel laser path to the hydrofoil, (c) Schematic diagram of holographic measurement principle.

1.3 Post-processing of hologram of mesoscopic bubble cluster

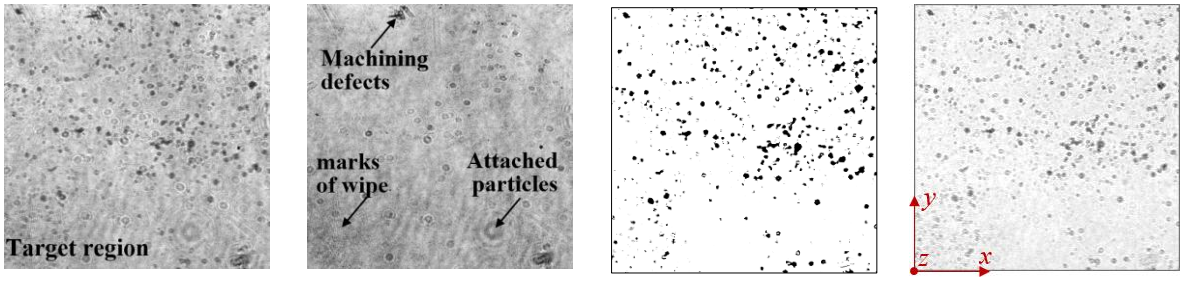
Fig. 3 depicts original holographic images captured of three distinct measurement locations at representative time instants. At location A, non-condensable gas bubbles carried by the free stream are relatively dispersed, exhibiting a low bubble number density. At location B, large-scale shedding clusters comprising discrete cavities of various sizes traverse the measurement volume above the hydrofoil. These structures cause significant obscuration of light and appear as aggregated cavity features in the holographic images. At location C, the shedding cloud detached from the trailing edge of the hydrofoil has fully collapsed, resulting in discrete microbubbles distributed throughout the entire holographic measurement volume. To enhance the computational efficiency of the post-processing, subsequent analysis is performed on specific regions of interest (ROIs) extracted from the original holographic images. These ROIs, delineated by white dashed boxes in Fig. 3, have dimensions of 800 × 800, 700 × 700, and 800 × 800 pixels for locations A, B, and C, respectively.



(a) inflow region (b) cavity shedding region (c) wake flow region

Fig.3. Original holographic of microbubbles in cavitating flow.

The reconstruction, bubble identification, and three-dimensional localization of DIH data adhere to the established processing pipeline described in prior works[61,61]. Initially, raw holograms are cropped to the region of interest, illustrated in Fig. 4(a). Because interference fringes in holograms arise not only from microbubbles but also from stationary optical defects, preprocessing is required to remove time-invariant background noise. This is achieved by averaging sequential holograms, as demonstrated in Fig. 4(b), to facilitate accurate microbubble feature extraction. Following acquisition of the background hologram, a cleaned hologram is produced by subtracting the background noise from the original holographic image, shown in Fig. 4(c). The cleaned hologram is subsequently normalized to improve the contrast of bubble interference fringes, presented in Fig. 4(d). Numerical reconstruction is conducted across a range of depths at 0.1 mm intervals through convolution with a diffraction kernel, effectively refocusing the hologram at various planes within the measurement volume. In-focus positions of bubbles are automatically identified using a minimum intensity criterion along the depth direction, as observed in Fig. 4(f), thereby obtaining their three-dimensional coordinates. A composite image is generated by selecting the minimum intensity value for each pixel across all reconstruction planes, shown in Fig. 4(g). This image is then binarized and processed using a Sobel operator to extract bubble edges for size determination, as depicted in Fig. 4(h).



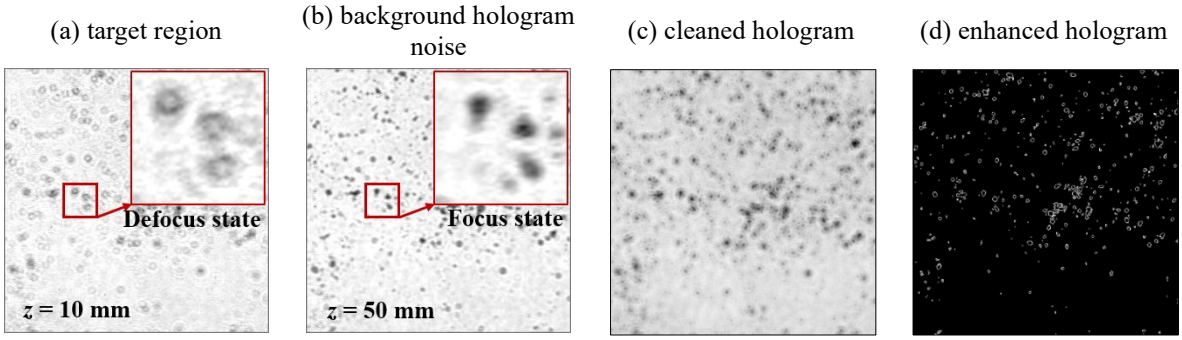
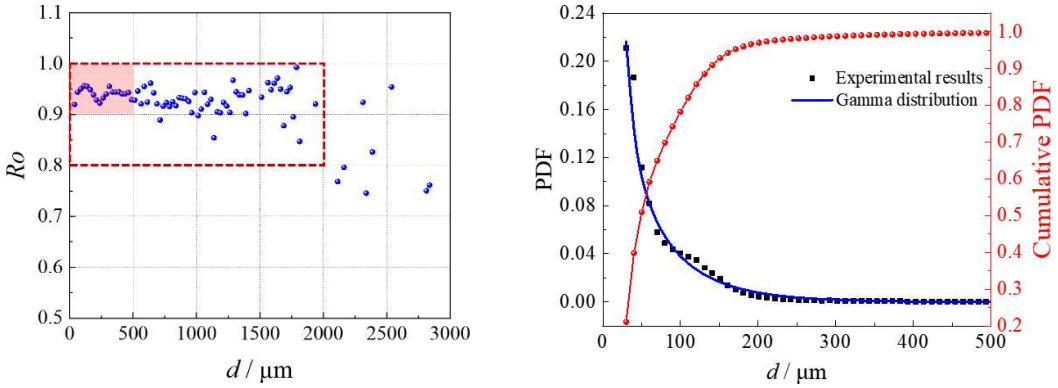


Fig. 4. Post-processing of bubble hologram.

Additionally, as indicated by prior research [62,63], the minimum particle size that can be effectively identified using holographic imaging is comparable to the pixel scale of high-speed cameras. Thus, this paper only conducts statistical analysis on discrete bubbles larger than 25 μm, which is equivalent to the pixel scale. Following the acquisition of the binarized combined hologram and the identification of bubble boundaries, the Roundness (R_O) of discrete bubbles obtained via holographic imaging can be calculated based on the perimeter and the pixel area enclosed by each bubble boundary. The Roundness is defined as:

$$R_O = \frac{c_b}{\sqrt{4\pi A}} \tag{3}$$

where c_b denotes the perimeter of the bubble boundary and A represents the total pixel area enclosed within the boundary. Fig. 5 shows the characteristics of bubble shape parameters and size distribution in wake flow region of cloud cavitation at σ = 1.4. Fig. 5(a) shows the distribution of bubble roundness along bubble diameter, while Fig. 5(b) presents the bubble size distribution. The vertical axis represents the average circularity of all bubbles within each size bin with 25 μm intervals, and the horizontal axis corresponds to the midpoint bubble diameter of each size bin. The equivalent bubble diameter is calculated based on the spherical bubble assumption using the formula $d = \sqrt{4A/\pi}$. As shown in Fig. 5(a), an increase in the equivalent diameter of discrete bubbles is associated with a reduction in roundness and greater variability in roundness values, suggesting that larger bubbles are more prone to deformation and tend to deviate from a spherical shape. Bubbles with diameters below 2000 μm consistently demonstrate roundness values above 0.8, as indicated by the red dashed rectangle. Smaller bubbles with diameters below 500 μm, highlighted by the red shaded region, exhibit roundness values strictly above 0.9, confirming that vapor structures within this size range can be considered spherical bubbles. Furthermore, Fig. 5(b) shows a rapid decrease in the bubble population with increasing bubble size, following a Gamma distribution, with nearly all discrete bubbles having diameters under 500 μm. These findings affirm the validity of the spherical bubble assumption for discrete vapor structures in the cavitating wake under the investigated cloud cavitation conditions.



(a) shape parameters of microbubbles in wake flow regions

(b) PDF and cumulative PDF of microbubbles in wake flow regions

Fig. 5. Characteristics of bubble shape parameters and size distribution in wake flow region of cloud cavitation.

However, the digitized contours of bubbles are significantly influenced by pixel discretization, particularly when the bubble diameter is comparable to or smaller than the imaging resolution. For instance, this effect becomes pronounced for microbubbles with diameters at or below 50 μm, which is close to twice the pixel size. To quantify the resulting impact and uncertainty on roundness measurements, we performed a Monte Carlo simulation. Ideal digital circles with a true roundness of 1.0 were generated, with diameters increasing from 1 to 20 pixels in increments of 0.25 pixels. Each circle was randomly shifted at a sub-pixel level to simulate arbitrary positioning within an image. After re-binarization and contour extraction, the measured roundness was computed. This process was repeated 1000 times for each diameter to determine the mean measured roundness, along with the corresponding standard deviation and relative error. Fig. 6 presents the Monte Carlo simulation evaluation results of the circularity values for bubble diameters measured under different conditions. When the diameter is below six times the pixel size (approximately 150 μm), a significant measurement error is observed, with a relative error exceeding 10%. As the diameter increases, the error decreases rapidly. For diameters larger than fifteen times the pixel size (approximately 375 μm), the measurement results show high agreement, with a relative error of less than 0.62%.

The evaluation demonstrates that extracting bubble contours from holographic images and calculating their circularity can effectively characterize the shape of larger-scale bubbles. This approach permits such bubbles to be treated as spherical for size quantification purposes. For bubbles with dimensions comparable to the pixel size, however, circularity-based morphological analysis exhibits considerable uncertainty. It is noted that under strong turbulent conditions, as bubble size decreases, the increasingly dominant isotropic surface tension promotes morphological stabilization. In such regimes, bubbles are more likely to retain a spherical shape, thereby supporting the applicability of spherical assumption even at smaller scales[64,65].

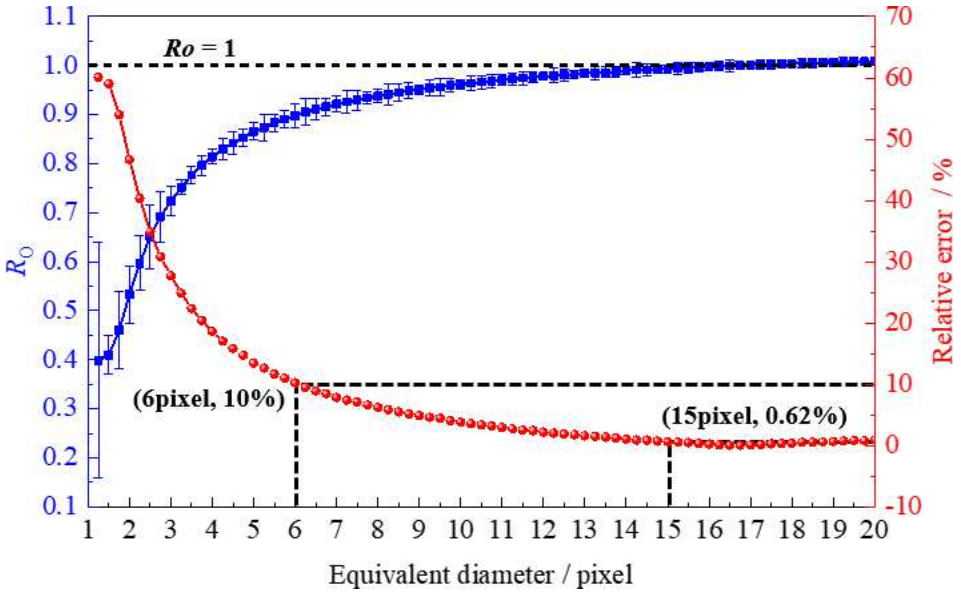


Fig. 6. Evaluation results of roundness values at different measured bubble diameters

As described previously, digital in-line holography was used to determine the spatial locations and sizes of mesoscopic bubble populations in a cavitating flow through sequential image processing, including enhancement, numerical reconstruction, and bubble boundary identification. Under the assumption of spherical bubbles, the three-dimensional structure of bubble clusters can be reconstructed using the obtained 3D coordinates and diameters of discrete microbubbles. Fig. 7 presents the instantaneous distribution of microbubbles acquired via digital in-line holography and processed using the numerical reconstruction method described earlier. As the detached cavity sheds into the holographic measurement volume, the large-scale cavity breaks up into numerous discrete microbubbles of smaller scales, which are dispersed non-uniformly throughout the wake region.

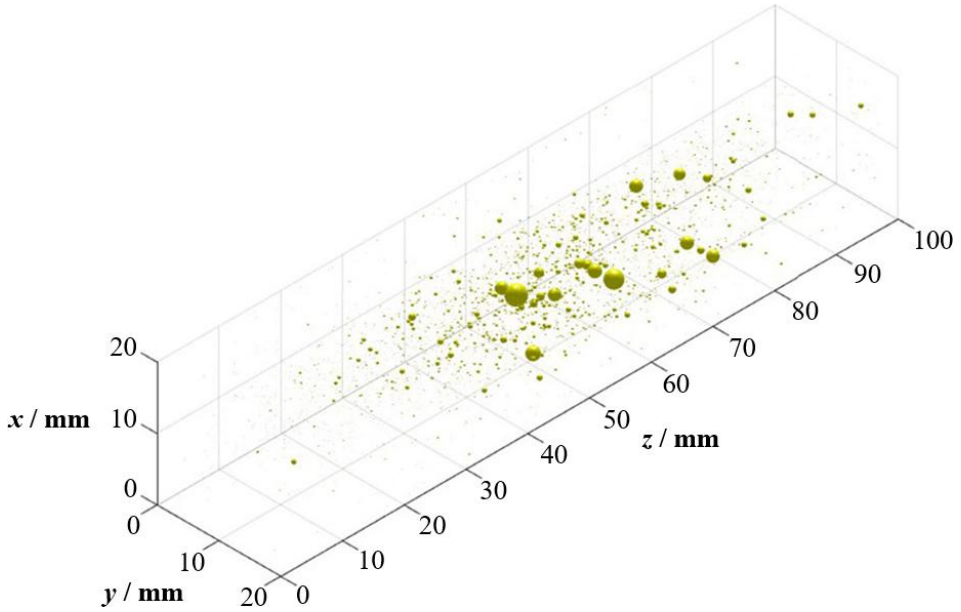
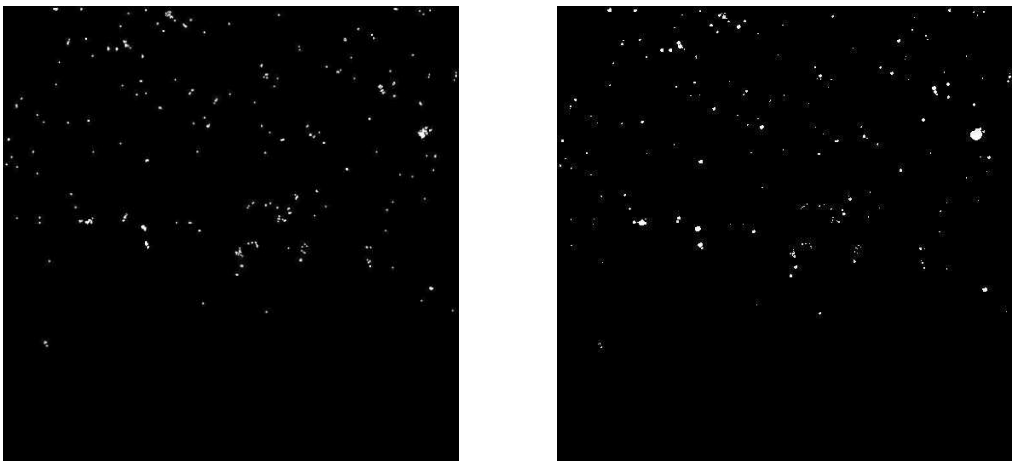


Fig. 7. Reconstruction of microbubble in wake flow region of cavitating flow at a typical instant.

Furthermore, Fig. 8 compares the numerically reconstructed result from the experimentally captured hologram at a typical instant with the binarized image obtained from the numerical reconstruction of mesoscale bubble clusters under the same viewing angle, where the white areas indicate the locations of

discrete bubbles. The results demonstrate that the numerical reconstruction method based on the spherical bubble assumption can effectively identify discrete bubbles within the holographic measurement region. Moreover, the bubble area fraction in the binarized image acquired via the digital in-line holographic measurement method is 0.41%, while that in the numerically reconstructed image corresponding to the experimental viewing angle is 0.39%, yielding a relative error of approximately 4.9%. This outcome verifies the reliability of the digital in-line holographic measurement and characterization method developed in this work for reconstructing mesoscale bubbles.



(a) Binarized image of the synthesized hologram

(b) Binarized image of the 2D numerical reconstruction

Fig. 8. Comparison of binarized images from microbubble holograph and numerical reconstruction

In light of the approximately isotropic turbulence within the cloud cavitation shedding region under high turbulence[37,66], the analysis in this work does not emphasize variations in the three-dimensional morphology of individual microbubbles. Moreover, to maintain consistency with the common practice in mainstream Eulerian–Lagrangian multiscale cavitation simulations[33,56], where discrete microbubbles are generally modeled as spherical entities, the present study treats discrete bubbles as spheres based on circularity analysis of their two-dimensional projection contours acquired through Digital In-line Holography (DIH). It should be noted, however, that this approach has inherent limitations in capturing the true three-dimensional shapes of discrete bubbles, particularly for larger microbubbles. Therefore, future work should focus on enhancing holographic processing algorithms, for example by introducing assumptions such as ellipsoidal fitting, to iteratively extract detailed information including the aspect ratio and spatial orientation of non-spherical bubbles.

2. Experiment results of multiscale cavity dynamics

2.1 *Morphological evolution of macroscale cavities in cloud cavitating flow*

Fig. 9 shows ten typical frames of one cycle of periodical cloud cavitation surrounding the NACA66 hydrofoil at an inflow velocity of U = 8.5 m/s and a cavitation σ = 1.4. The initial time for a cycle of periodic cloud cavitation is set to the moment when cavitation inception occurs at the hydrofoil leading edge. As shown in Fig. 9, between t_0 = 1 ms and t_4 = 13 ms, a large-scale attached cavity develops and extends downstream from the leading edge to the mid-chord region of the hydrofoil. During the growth of attached cavity, the vapor-liquid structure remains optically transparent interface, while the flow regions adjacent to the wall exhibit increased instability. At the instant of t_5 = 17 ms, the large-scale cavity develops further downstream. Simultaneously, a re-entrant jet originates from the cavity closure region and propagates upstream along the suction surface, inducing violent fluctuations in the attached cavity and causing the cavity interface to become blurred. When the re-entrant jet reaches the leading edge of hydrofoil at t_6 = 21 ms, the large-scale cavity extends to the trailing edge of the hydrofoil, and its length

attains the maximum value. Subsequently, from t_6 = 21 ms to t_{10} = 37 ms, the detached largescale cavity gradually converges into an opaque misty cloud characterized by its gradual collapse while being shed downstream, resulting in a decrease in the cloud cavity volume. Concurrently, the inception and growth of the attached cavity for the subsequent cycle occurs on the suction surface, extending to the rear part of hydrofoil. It should be noted that the application of high-speed photography for full-field observation of cavitating flows is constrained to characterizing the dynamics of large-scale cavities. The quantification of finer-scale bubble structures within the two-phase region, especially in the interior of shedding cloud cavities, is hindered by the adverse effects of limited spatial resolution and inter-cluster occlusion.

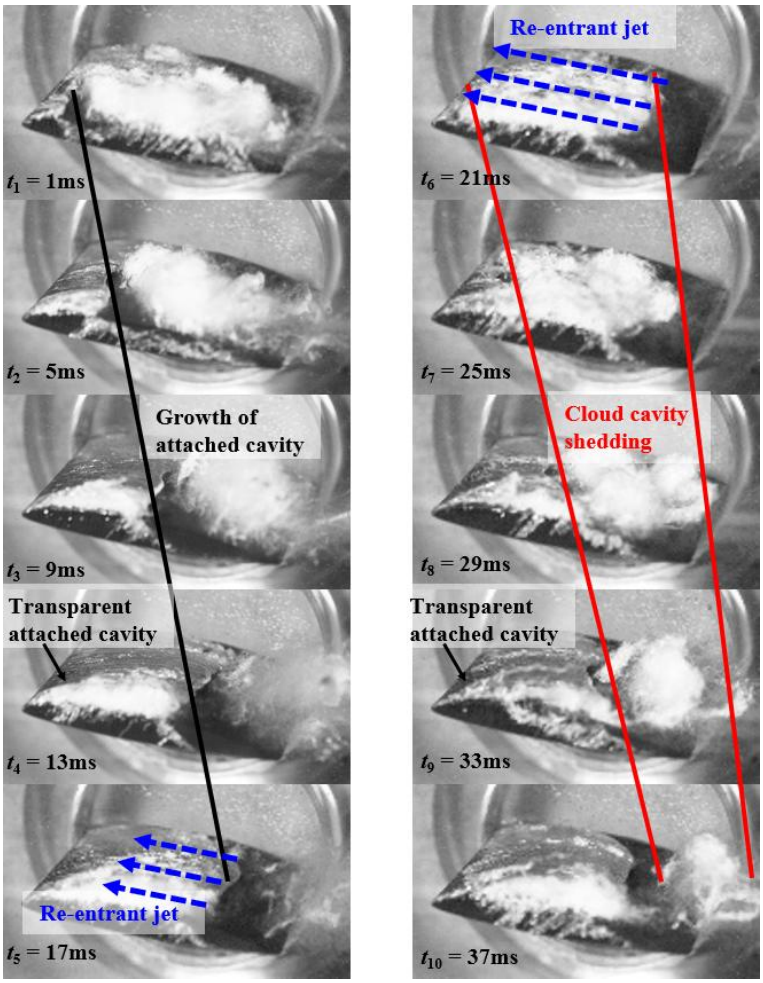


Fig. 9. Dynamic evolution of cavities in cloud cavitating flow at σ = 1.4.

2.2 *Transient evolution characteristics of microbubbles in cloud cavitating flow*

Based on digital in-line holography, Fig. 10 presents the variation curve of the spatial number density of cavitation nuclei in the incoming flow and the Sauter mean diameter (SMD) over a 100 ms period at an inflow velocity of U = 8.5 m/s and cavitation number of σ = 1.4. The SMD is commonly used to characterize the average size of a discrete microbubble population and is defined as:

$$d_{32} = \sum_{i=1}^{n} d_i^3 / \sum_{i=1}^{n} d_i^2 \tag{4}$$

The results indicate that due to the free-stream flow not being subjected to strong disturbances before reaching the hydrofoil, both the number density and SMD of microbubbles within the field of view of the holographic measurement exhibited minimal fluctuations over time. The time-averaged microbubble

number density in the inflow region is about 0.84×10^7 per cubic meter, and the time-averaged SMD is about 191.67 μm.

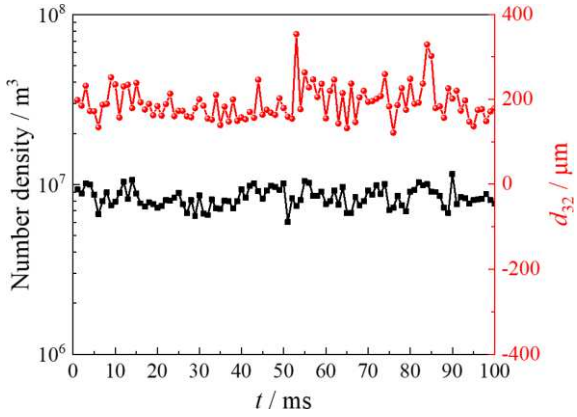


Fig. 10. Transient evolution characteristics of microbubbles in inflow region.

Fig. 11 presents the transient evolution characteristics of discrete bubbles within the cavity shedding region at the mid-rear section of the hydrofoil, as captured through holographic measurements. For cloud cavitating flow around hydrofoil an inflow velocity of U = 8.5 m/s and cavitation number of σ = 1.4. Under the influence of the re-entrant jet, large-scale shedding clouds periodically pass through the holographic measurement region at the mid-rear section upon the hydrofoil, resulting in quasi-periodic fluctuations in both the spatial number density of discrete cavitation bubbles and the average bubble diameter within the measured field, as shown in Fig. 11(a). The time-averaged microbubble number density in the inflow region is about 9.4×10^7 per cubic meter, and the time-averaged SMD is about 247.16 μm. To further investigate the influence of the cloud cavitation evolution process at the mid-rear section of the hydrofoil on the detectable discrete microbubbles, Fig. 11(b) presents a detailed view of the data within the blue dashed rectangle marked in Fig. 11(a), corresponding to a full evolution cycle. The results demonstrate that within a full evolution cycle, the population of discrete microbubbles initially increases and then decreases, while the SMD does not exhibit a similar periodic pattern. Three typical time instants, labeled B-I, B-II, and B-III, are selected from Fig. 11(b) to analyze multiscale cavitation evolution patterns. As shown in the image corresponding to B-I in Fig. 11(c), when the shedding cloud cavity enters the measurement field of the holographic system, the laser path cannot penetrate the dense bubble cluster. Numerous discrete bubbles are dispersed around the shedding cloud cavity, and these can be effectively reconstructed through holographic measurement techniques. At the time instant of B-II, as the smaller-scale shedding cavitation cloud moves downstream away from the holographic measurement region, the number of dispersed bubbles increases significantly. At the time instant of B-III, when obstruction of the light path by the small-scale shedding cloud is minimal, the measurable population of discrete bubbles reaches its maximum. Moreover, it should be noted that the decrease in bubble density observed in the cavitation shedding region in Fig. 11 may be partly attributed to optical occlusion effects rather than to the physical absence of bubbles in that region. Probe-based measurements have confirmed that the cloud cavities shedding from the suction surface and moving into the wake flow of the hydrofoil are not continuous vapor phases but consist of millimeter-scale dense bubble clusters[37]. However, when such cloud cavities enter the holographic measurement area, the high gas content inside and mutual obstruction among bubbles significantly reduce laser penetration, leading to the failure of the holographic measurement method adopted in this study. As a result, the transient evolution curve of the discrete bubble number density in Fig. 11 exhibits periodic fluctuations; once the cloud cavity fully enters the holographic light path, the discrete bubbles inside cannot be effectively detected due to the method's

limitations, causing the number density to drop to its minimum. Additionally, the widely used high-fidelity Large Eddy Simulation (LES) coupled with the Volume of Fluid (VOF) method can well represent the large-scale discontinuous cavity structures inside cloud cavities, yet it struggles to resolve the discrete microbubbles distributed near the cavity boundaries. Therefore, the discrete bubble data in the cavitation shedding region obtained through holography in this study can serve as a valuable supplement to existing numerical simulation results, providing reference and validation for the improvement of multi-scale cavitation modeling methods.

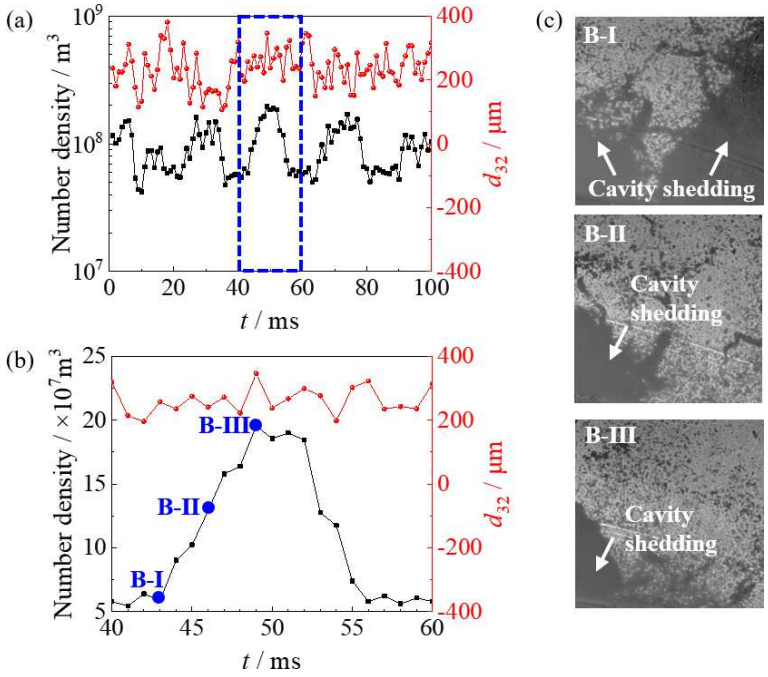


Fig. 11. Transient evolution characteristics of microbubbles in cavity shedding region. (a) Time evolution of discrete bubble number density and sauter mean diameter, (b) Time evolution of discrete bubble number density and sauter mean diameter in typical cavitation cycle, (c) Holographic image of a typical moment.

At measurement position C, the evolutionary characteristics of discrete microbubbles within the wake flow region cloud cavitating flow around the hydrofoil are investigated using digital in-line holography. Fig. 12(a) presents the temporal evolution of both the spatial number density of discrete microbubbles and the SMD within the target measurement region over a period of 100 ms. Within the field of holographic measurement, the spatial number density of discrete bubbles exhibited periodic fluctuations, while the Sauter mean diameter of the bubble population showed minimal variations. Furthermore, during the measured period, the time-averaged bubble number density in the cavity shedding region was 6.9×10^7 per cubic meter, with a time-averaged SMD of 235.63 μm. Compared to the cavity shedding region at the mid-rear section of the hydrofoil suction side, both the spatial number density and the average diameter of discrete bubbles in the cavitating wake region show a noticeable decrease. This reduction can be attributed to the higher ambient pressure and stronger turbulent intensity in the wake region, where the population of mesoscopic bubbles undergoes active break-up, contraction, and collapse processes. As shown in Fig. 12(b), the population of discrete bubbles demonstrates a characteristic pattern of initial increase followed by decrease during one complete evolution cycle. Furthermore, as illustrated in Fig. 12(c), three representative time instants, namely C-I, C-II, and C-III, are selected from the holographic image sequences for detailed analysis of the spatiotemporal evolution characteristics of mesoscopic bubbles. The holographic image at time C-I reveals that when the shedding

cavitation cloud moves into the holographic measurement region near the trailing edge of the hydrofoil, the cloud cavity completely breaks up and disperses into numerous microbubbles under the influence of intense turbulent flow. At time C-II, as the shedding cavitation cloud moves further downstream away from the measurement region, the number of dispersed bubbles gradually decreases. By time C-III, the shedding cavitation cloud has completely moved out of the observational field of view of the holographic system, and the measurable population of discrete bubbles reaches its minimum.

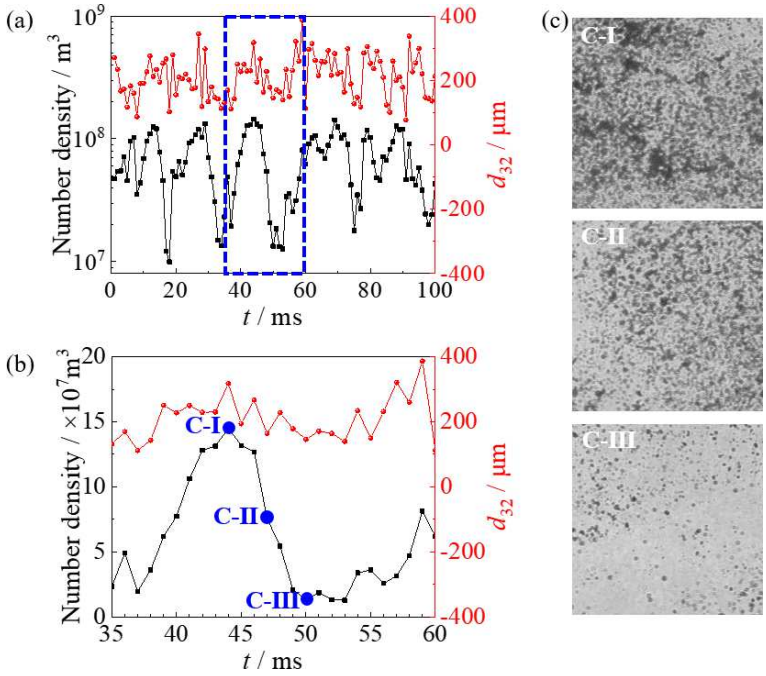
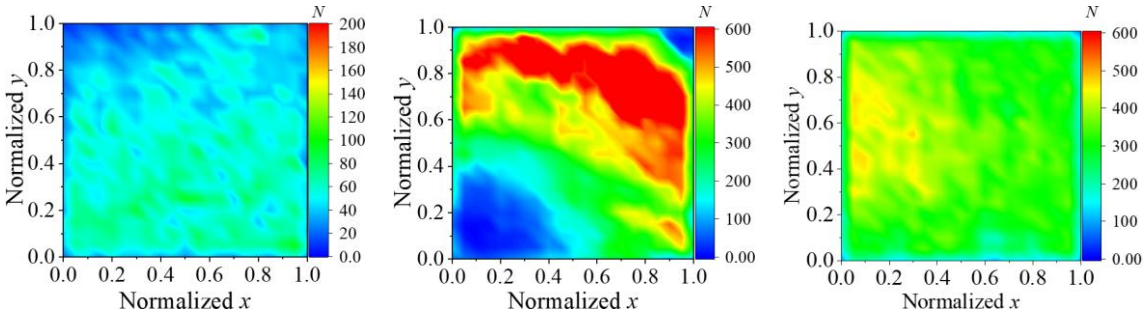


Fig.12. Transient evolution characteristics of microbubbles in wake flow region. (a) Time evolution of discrete bubble number density and sauter mean diameter, (b) Time evolution of discrete bubble number density and sauter mean diameter in typical cavitation cycle, (c) Holographic image of a typical moment.

2.3 *Statistical characteristics of microbubbles in cloud cavitating flow*

Fig. 13 presents time-averaged spatial distribution contours of mesoscale discrete bubbles at different measurement locations in the cloud cavitating flow around a NACA66 hydrofoil. The coordinates in the figure are normalized by the corresponding width of the target region in the holograms. With a normalized spatial resolution of 0.001 × 0.001, the number of discrete bubbles at each location is quantified to analyze the statistical characteristics of their spatial distribution within the holographic laser illumination region. Fig. 13(a) shows the free-stream region, where the turbulent intensity is relatively low, resulting in a low number density of cavitation nuclei uniformly distributed across the measurement area. In contrast, Fig. 13(b) depicts the cavity shedding region from the mid-chord to the trailing edge of the hydrofoil. Within the holographic measurement zone, large-scale cavity structures are concentrated in the lower-left region near the suction side. The number density of discrete bubbles increases gradually in both the streamwise and vertical directions, which is attributed to the high velocity gradients and strong density gradients near the edges of the shedding cavity. There, intense turbulence enhances vapor-liquid mixing, promoting the generation of numerous discrete bubbles. As shown in Fig. 13(c), discrete bubbles are distributed across the entire measurement area in the cavitating wake region. The distribution is relatively uniform in the vertical direction, but the number of bubbles decreases rapidly in the streamwise direction. In this region, the large cloud cavities have completely broken down, and the bubbles gradually collapse and vanish as they are shed downstream.



(a) inflow region (b) cavity shedding region (c) wake flow region

Fig.13. Time-average space number density of microbubble.

Fig. 14 shows the number density of microbubbles at various measurement locations within the cloud cavitating flow, as obtained from holographic measurements. The probability distribution of microbubble counts across different diameters represents time-averaged values derived from five repeated experimental trials, each comprising 1000 instantaneous snapshots per holographic observation, and the error bars are calculated using the standard deviation. It should be noted that all microbubbles detected via holography in both the cavity shedding region and the wake flow region comprise not only vapor bubbles formed by the collapse of periodically detached large-scale cavities but also include cavitation nuclei present in the inflow. The results indicate that within the cavitation region, the population of microbubbles across multiple scales increases significantly. Consistent with previous findings obtained through numerical simulations and probe-based experimental measurements, the size distribution of microbubbles follows a power-law behavior[37,66]. Specifically, the distribution for smaller bubbles is dominated by the -4/3 power law, while that for larger microbubble population conforms to the -10/3 power law.

The observed size distribution exhibits parallel with that of air bubbles entrained by breaking waves, as reported in both laboratory and open ocean. This distribution depends on bubble size and the turbulence of the carrier flow. Although the two flow regimes differ fundamentally, their bubble size spectra share similar power-law exponents. This similarity suggests common underlying mechanisms, in which small bubbles detach from macroscopic structures and break up into clusters via multiscale vortices. Therefore, insights from bubble formation in breaking waves can provide some guidance for investigating the physical mechanism governing the observed power-law scaling in bubble size distributions in cavitating flow.

The scaling exponent for larger bubbles in wave breaking, accounting for buoyancy and dissolution, typically ranges from -2.5 to -3.5[64]. In the context of cavitating flow, gravitational effects are negligible because turbulent accelerations imposed on microbubbles far exceed gravitational acceleration[67]. Furthermore, the aggregation of discrete bubbles can be disregarded, as the contact time and Weber number associated with microscale bubbles are orders of magnitude smaller than the relevant liquid film drainage time and the critical Weber number in turbulent cavitation[67]. Given that bubbles interact most strongly with eddies of comparable size [68], the complex turbulent vortex cascade drives larger bubbles to rapidly fragment into multiple smaller daughter bubbles. Dimensional analysis shows that this fragmentation process can give rise to the characteristic -10/3 scaling observed in the larger-bubble size spectrum of cavitating flow[64].

Along with the successive turbulent energy cascade, bubbles undergo a parallel fragmentation cascade，leading to an exponential increase of discrete bubble number as the bubble size decreases[69]. When discrete microbubbles break down to a sufficiently small scale, a relative equilibrium is reached between the bubble surface energy and the local turbulent energy, allowing microbubbles to persist stably

within the turbulent field. Once the surrounding flow conditions change, these discrete bubbles will correspondingly adjust in size, either growing, shrinking, or collapsing. The minimum surface energy of the relative stable microbubble with diameter d, $E_b(d)$, is equal to $(\sigma/\rho)\pi d^2$. The number of bubbles with diameter d per unit volume is $N(d)$. Thus, the total surface in per unit volume is $N(d)\cdot(\sigma/\rho)\pi d^2$. Meanwhile, it is known that the turbulence at scale $1/k$ is the main reason for generating bubbles at scale d~$1/k$[70]. Therefore, the turbulent kinetic energy density can be evaluated as $0.5\rho u'^2$. For turbulent cavitating flow, the cavitation-turbulence interaction motives an essentially isotropic turbulence, which provides the turbulence energy spectrum as the Kolmogorov spectrum[66]. So that, the fluctuating velocity can be described as $u'^2 \propto \varepsilon^{2/3} d^{2/3}$. Therefore, the kinetic energy of turbulent cavitating flow is about $0.5\rho\varepsilon^{2/3}d^{2/3}$. Finally, based on the assumption that the turbulent kinetic energy per unit volume is comparable to the total surface energy of the bubble population, the slope of bubble number density across bubble size yields as $N(d) \propto d^{-4/3}$.

The critical bubble size that differentiates these two regimes is given by the Hinze scale[68], which establishes the criterion for bubble breakup from a balance between disruptive anisotropic pressure fluctuations and restorative surface tension forces. Besides, the previous study demonstrated that from the freestream to the cavitating wake region behind the hydrofoil, the turbulence intensity increases along the streamwise direction, leading to a gradual growth in the Hinze scale[66]. In the present work, the holographic measurements of microbubbles reveal the same trend of the Hinze scale. In the inflow region, the Hinze scale is considerably smaller, measuring approximately 70 μm. However, within the cavity shedding zone and the cavitating wake region, the critical scale demarcating different power-law regimes is observed to be approximately 140 μm.

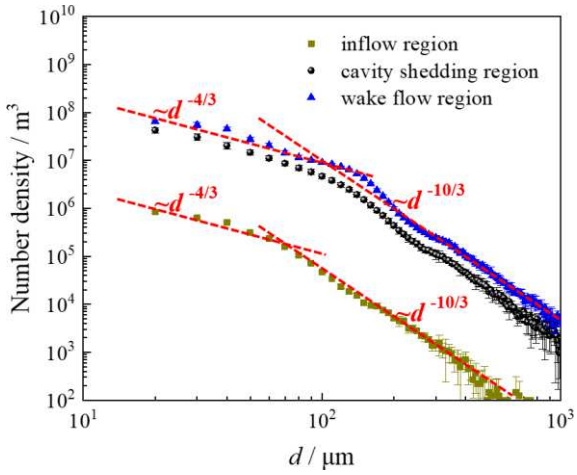


Fig.14. bubble size distribution of cloud cavitating flow at different measurement location.

The quantitative data of discrete microbubbles in the above typical cloud cavitating flow serve as key modeling parameters, providing data support for the subsequent optimization of the Eulerian–Lagrangian multiscale cavitation model. It should be noted that when environmental conditions change, the spatiotemporal distribution characteristics of discrete bubbles in the cavitating flow field will also change accordingly. In another recent study conducted in the same recirculating cavitation water tunnel using the same NACA66 hydrofoil as in this paper, holographic measurements were performed under the condition of inflow velocity U = 9 m/s. The results show that in the inflow region, the spatial number

density, Sauter mean diameter, and bubble size distribution characteristics of non-condensable gas bubbles vary little with the cavitation number, with the relevant data and average scale showing only minor temporal fluctuations. In contrast, within the cavity-occupied zone, holographic data reveal that as the cavitation number decreases, the spatial number density of discrete bubbles increases significantly, accompanied by a pronounced amplification of temporal fluctuation amplitudes. Notably, across all conditions examined, the size distribution of discrete microbubbles exhibits a well-defined dual power-law scaling, delineated by the Hinze scale. Specifically, microbubbles below the Hinze scale follow a −4/3 power law, whereas those above the Hinze scale obey a −10/3 scaling. The results indicate that the dual power-law distribution characteristics of bubble size revealed earlier under the condition of $\sigma = 1.4$ are not an isolated phenomenon specific to that operating condition, but rather reflect a common statistical law governing the evolution of bubble populations across a relatively wide operational range from cavitation inception to cloud cavitation. The power-law exponents exhibit no statistically significant dependence on the cavitation number. This insensitivity occurs because the scaling is fundamentally governed by the statistical balance between turbulent breakup and surface tension, a physical law that remains invariant across the cavitation numbers studied[37,64,66]. Nevertheless, it is important to emphasize a discernible shift observed in the transition scale between the two distribution regimes when comparing results obtained under different flow velocities while maintaining the same cavitation number. Specifically, under the condition of $\sigma = 1.4$, increasing the inflow velocity from 8.5 m/s, as studied in this work, to 9 m/s leads to a measurable change in the transition scale. This shift can be attributed to the close dependence of the transition scale on the turbulent intensity of the cavitating flow. Variations in inflow velocity may substantially alter cavitation dynamics even at identical cavitation numbers, a phenomenon that will constitute a key focus of our subsequent experimental investigations. Current research has well established that variations in inflow velocity significantly influence cavitation morphology and hydrodynamic characteristics at the macroscopic scale[71]. However, at the mesoscopic scale, the specific mechanisms through which inflow velocity alone affects discrete bubble behavior remain insufficiently understood. This study will subsequently undertake a systematic analysis to address this issue.

3. Multiscale model considering bubble features from experimental measurement

As a typical multiphase turbulent flow, cavitating flow exhibits significant multiscale characteristics in its dynamic evolution process. In the previous section, the spatiotemporal evolution of multiscale cavitating bubbles was captured using digital in-line holography, and quantitative statistics on the content of cavitation nuclei in the flow field were obtained. Building upon these experimental measurements of multiscale cavitation, this section will further optimize an unsteady cavitation simulation method based on Eulerian–Lagrangian coupling by comprehensively accounting for the influence of non-condensation bubble in inflow region on cavitation simulation. As shown in Fig. 15, the continuous-phase flow field of cavitating flow is simulated in the Eulerian framework based on the homogeneous assumption by solving the Navier-Stokes equations, with the Volume of Fluid (VOF) method employed to capture the vapor-liquid interface of largescale cavities. Meanwhile, the transport and growth of mesoscale non-condensation bubbles carried in the incoming flow and microscale vapor bubbles are modeled in the Lagrangian framework using the Discrete Bubble Model (DBM). To address cross-scale phenomena, including the rupture of macroscopic cavities during re-entrant jet propagation and cloud cavity shedding, as well as the coalescence of microbubbles, a two-way coupling and conversion algorithm between the Eulerian continuous phase and the Lagrangian discrete phase is developed for high-fidelity numerical simulation. The specific computational methods illustrated in the figure will be detailed in the subsequent

sections.

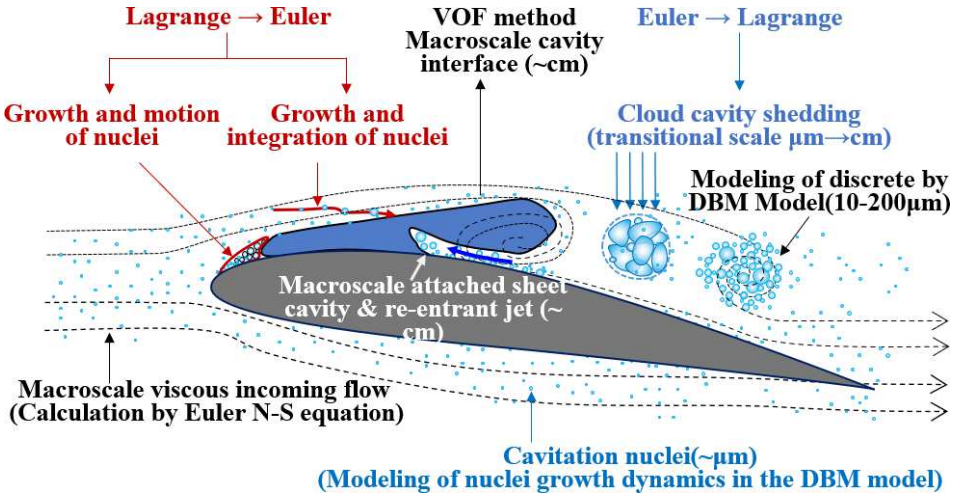


Fig.15. Schematic of multiscale cloud cavitating flow characteristics and numerical modeling in Euler-Lagrange frame.

3.1 *Governing equations of fluid flow*

In this study, the vapor and liquid phases are treated as a thermodynamically equilibrium homogeneous mixture. Meanwhile, the large eddy simulation (LES) model is adopted to directly resolve large-scale turbulent coherent structures while modeling subgrid-scale (SGS) turbulence through appropriate stress models, which allows high-fidelity representation of multiscale turbulent coherent structures in cavitating flows within computationally feasible limits. The governing equations for the continuous flow field, namely the mass and momentum conservation equations, are formulated as follows:

$$\frac{\partial \rho_m}{\partial t}+\frac{\partial(\rho_m \bar{u}_i)}{\partial x_i}=0 \tag{5}$$

$$\frac{\partial(\rho_m \bar{u}_i)}{\partial t}+\frac{\partial(\rho_m \bar{u}_i \bar{u}_j)}{\partial x_j}=-\frac{\partial \bar{p}}{\partial x_i}+\frac{\partial}{\partial x_j}(\mu_{\mathrm{m}}\frac{\partial \bar{u}_i}{\partial x_j})-\frac{\partial \tau_{ij}}{\partial x_j}+\rho_m g_i+S_b+F_s \tag{6}$$

where u_i represents the velocity components in the three directions within the Eulerian framework (where i denotes the x, y, and z directions), p denotes the flow field pressure, F_s refers to the surface tension at the vapor-liquid interface, and S_b represents the momentum source term induced by discrete bubbles. Additionally, ρ_m denotes the mixture density, and μ_m signifies the dynamic viscosity of the mixture.

$$\rho_m=\rho_l\alpha_l+\rho_v\alpha_v \tag{7}$$

$$\mu_m=\mu_l\alpha_l+\mu_v\alpha_v \tag{8}$$

where α represents the volume fraction of each phase within a local Eulerian control volume, and the subscripts v and l denote the vapor and liquid phases, respectively, for the respective flow field variables.

In addition, the subgrid-scale stress, τ_{ij}, is defined as:

$$\tau_{ij}=\rho_m\left(\overline{u_i u_j}-\bar{u}_i\bar{u}_j\right) \tag{9}$$

The subgrid-scale stress, which cannot be directly resolved within the Eulerian framework is modeled as:

$$\tau_{ij}-\frac{1}{3}\tau_{kk}\delta_{ij}=-2\mu_t\overline{S_{ij}} \tag{10}$$

Among these, μ_t denotes the turbulent viscosity, and τ_{kk} represents the isotropic stress term. The symbol $\overline{S_{ij}}$ refers to the strain-rate tensor at the resolved scale, defined as follows:

$$\overline{S_{ij}}=\frac{1}{2}\left(\frac{\partial\overline{u_i}}{\partial x_j}+\frac{\partial\overline{u_j}}{\partial x_i}\right) \tag{11}$$

Meanwhile, the sub-grid scale model of Wall-Adapting Local Eddy-Viscosity (WALE) [72] is employed to compute the turbulent viscosity μ_t:

$$\mu_t=\rho L_s^2\frac{\left(S_{ij}^d S_{ij}^d\right)^{3/2}}{\left(\overline{S_{ij}S_{ij}}\right)^{5/2}+\left(S_{ij}^d S_{ij}^d\right)^{5/4}} \tag{12}$$

$$S_{ij}^d=\frac{1}{2}\left(\overline{g}_{ij}^2+\overline{g}_{ji}^2\right)-\frac{1}{3}\delta_{ij}\overline{g}_{kk}^2 \tag{13}$$

$$\overline{g}_{ij}=\frac{\partial\overline{u}_i}{\partial x_j} \tag{14}$$

$$L_s=\min\left(\kappa l_d, C_s\Delta\right) \tag{15}$$

where L_s is the mixing length, κ denotes the von Kármán constant, l_d represents the distance to the nearest wall, and C_s is the model constant with a value of 0.325. Δ denotes the local grid scale, defined as:

$$\Delta_{grid,3D}=\left(\Delta x\cdot\Delta y\cdot\Delta z\right)^{1/3} \tag{16}$$

where Δx, Δy, and Δz are the grid scales in the three coordinate directions of the current computational cell within the Eulerian framework.

3.2 *Macroscale model for large cavities*

In the multiscale numerical simulation of cavitating flows, in addition to the construction of an appropriate turbulence closure model, the refined description of the topological structure of the phase interface is particularly crucial. This paper employs the Volume of Fluid (VOF) method based on a fixed Eulerian grid. By calculating the volume fraction of each phase within the computational cells, the position and orientation of the interface are determined from the phase distribution, enabling high-precision capture of the vapor/liquid two-phase interface. The transport equation for the vapor phase volume fraction in the cavitating flow field is defined as:

$$\frac{\partial(\rho_v\alpha_v)}{\partial t}+\frac{\partial(\rho_v\alpha_v u_j)}{\partial x_j}=\dot{m}^-+\dot{m}^++S_v \tag{17}$$

where S_v is the mass source term induced by discrete bubbles, $\dot{m}^-$ and $\dot{m}^+$ present the condensation rate and vaporization rate of vapor phase, respectively. In present work, the Schnerr–Sauer model is employed to govern the interphase mass transfer between vapor and liquid. The rate of vaporization and condensation governing the mass exchange between the liquid and vapor phases can be mathematically formulated as:

$$\begin{cases} \dot{m}^{+}=\dfrac{3\alpha_v(1-\alpha_v)}{R_B}\dfrac{\rho_v\rho_l}{\rho}\sqrt{\dfrac{2}{3}\dfrac{P_v-P}{\rho_l}}, P<P_v \\ \dot{m}^{-}=\dfrac{3\alpha_v(1-\alpha_v)}{R_B}\dfrac{\rho_v\rho_l}{\rho}\sqrt{\dfrac{2}{3}\dfrac{P-P_v}{\rho_l}}, P\geq P_v \end{cases} \tag{18}$$

3.3 *Discrete bubble model*

To track the motion of individual bubbles, the Newtonian equations of motion are solved, taking into comprehensive consideration the various hydrodynamic forces acting on the bubbles:

$$\frac{du_b}{dt}=F_D+F_{buo}+F_{VM}+F_{PG} \tag{19}$$

The terms on the right-hand side of Eq. (19) represent, respectively, the drag force [73], body force, added mass force [74], and pressure gradient force [75] acting on the mesoscopic bubble in the flow field.

The drag force acting on discrete bubbles within the field of a transient cavitating flow is defined as:

$$F_D=C_D\frac{3}{4d_b}\frac{\rho_l}{\rho_b}(u_l-u_b)|u_l-u_b| \tag{20}$$

where the subscripts *l* and *b* denote the continuous flow field and discrete bubble, respectively. The drag coefficient C_D for a discrete bubble in a cavitating turbulent flow can be expressed as [76]:

$$C_D=\begin{cases} 24/Re_p, & Re_p<0.1 \\ 24/Re_p\left(1+0.15\,Re_p^{0.687}\right), & 0.1\leq Re_p\leq 1000 \\ 0.44, & Re_p>1000 \end{cases} \tag{21}$$

where the bubble Reynolds number, R_{ep}, is defined as:

$$Re_p=\rho_l d_b|u_l-u_b|/\mu_l \tag{22}$$

where d_b is the diameter of the discrete bubble, u_b denotes the velocity vector of the discrete bubble, and u_l represents the velocity vector of the carrier fluid surrounding the bubble.

The volumetric force on the bubble incorporates the combined mechanical effects acting on the discrete bubble, such as gravity and buoyancy, which is defined as:

$$F_{buo}=\rho_l V_b g\frac{\rho_l-\rho_b}{\rho_b} \tag{23}$$

The virtual mass force, a key dynamic parameter in two-phase flow interactions, originates physically from the inertial coupling effect between phases under accelerated motion. Particularly when bubbles traverse regions with strong velocity/pressure gradients, such as shocks or vortex cores, the dynamic coupling between the virtual mass force and the pressure gradient force leads to a lag in bubble migration velocity and induces interfacial wave instability. This study establishes an asymmetric added mass tensor model to elucidate the motion characteristics of discrete bubbles in highly transient flow fields. The virtual mass force is defined as:

$$F_{VM}=C_{VM}\rho_l V_b\left(\frac{Du_l}{Dt}-\frac{du_b}{dt}\right) \tag{24}$$

In the equation, C_{VM} is assigned a value of 0.5, representing the virtual mass force coefficient, and V_b is defined as the volume of the discrete bubble.

The pressure gradient force acting on a discrete bubble due to a non-uniform pressure distribution over its surface is defined as:

$$F_{PG} = u_b \frac{\rho_l}{\rho_b} \frac{\partial u_l}{\partial x} \tag{25}$$

The growth and collapse processes of discrete bubbles originating from the rupture of largescale shedding cavities are simulated using a simplified Rayleigh-Plesset equation:

$$\frac{dR_b}{dt} = sign(P_v - P)\sqrt{\frac{2}{3}\left(\frac{|P_v - P|}{\rho_l}\right)} \tag{27}$$

The simplified bubble dynamics model retains only the first-order terms of the Rayleigh–Plesset equation while neglecting second-order terms and surface tension effects. To compensate for these simplifications, correction coefficients C_{vap} and C_{cond} are introduced to modulate the rates of bubble growth and collapse, respectively. Furthermore, since cavitation nuclei may exist even in regions where pressure exceeds the saturated vapor pressure, a saturated pressure coefficient C_{sp} is incorporated to better represent the nucleation process. The product $C_{\text{sp}} \cdot P_v$ is defined as the nucleation pressure.

Accordingly, the bubble growth and collapse rates can be expressed as:

$$\frac{dR_b}{dt} = \begin{cases} sign\left(C_{sp}p_v - p\right)C_{vap}\sqrt{\frac{2}{3}\left(\frac{C_{sp}p_v - p}{\rho_l}\right)} \\ sign\left(C_{sp}p_v - p\right)C_{cond}\sqrt{\frac{2}{3}\left(\frac{C_{sp}p_v - p}{\rho_l}\right)} \end{cases} \tag{28}$$

In the multiscale cavitating flow numerical method developed in this study, the model parameters are set as follows C_{vap}=0.5、C_{cond}=0.001 and C_{sp}=1.3.

Regarding of the non-condensable gas bubbles carried into the cavitating flow field by the incoming flow from upstream, the growth and variation of their bubble radius follow the ideal gas law:

$$pV = nRT = Const \tag{29}$$

where p is the freestream ambient pressure, V is the volume of the non-condensable bubble, n is the number of molecules contained within the non-condensable bubble, R is the universal gas constant equal to 8.31J/(mol·K), and T is the freestream temperature set at 300 K. Therefore, when the non-condensable bubble moves into other regions of the flow field, the radius can be calculated by:

$$R = \left(\frac{p}{p_{local}}\right)R_0 \tag{30}$$

where p_{local} refers the local pressure in continuous flow and R_0 is the initial radius of non-condensable bubble.

3.4 *Two-way transition algorithm*

A robust strategy for transitions between Eulerian and Lagrangian frameworks is essential for multiscale cavitation simulations. The two-way coupling algorithm, illustrated in Fig. 16, iterates between solving the continuum flow field and tracking discrete bubble dynamics within each time step. The procedure begins by solving the Eulerian conservation equations for mass, momentum, and species transport, employing the PISO algorithm for pressure-velocity coupling to determine the velocity, pressure, and phase fraction fields. Subsequently, the non-condensation bubbles and mesoscale vapor bubbles are introduced stochastically into inflow region and sub-grid low pressure regions, respectively. The Lagrangian tracking of microbubbles is then performed by integrating their motion and growth governing equations. Scale transition occurs when a microbubble nears the macroscopic interface as

volume of vapor (α_v) in the local computational cell exceeds the threshold of 0.65, or exceeds a critical microbubble diameter, leading to its assimilation into the Eulerian continuum via the VOF method. Interphase coupling is enforced by incorporating corresponding mass and momentum source terms into the continuous-phase equations[15–17], followed by a convergence check for both phases before advancing in time.

The mass source term S_v in Eq. (17) represents the contribution of a removed bubble to the Eulerian continuous field and is given by

$$S_v = \frac{V_B}{V_{cell}\Delta t} \cdot \rho_v \tag{31}$$

where V_B is the volume of the removed bubble, V_{cell} is the volume of the local computational cell, Δt is the time step size, and ρ_v is the density of the vapor phase.

Additionally, large-scale cavities are treated within the Eulerian framework, while small-scale bubbles are tracked using a Lagrangian approach. Consequently, the vapor volume fraction must be updated for the subsequent iteration of the continuous field solution as follows:

$$\alpha_v' = \alpha_v + \frac{\sum V_{b,j}}{V_{cell,i}} \tag{32}$$

where i denotes the index of the flow field solution unit, j denotes the index of the discrete bubble within that unit, and the α_v' denotes the vapor volume value for the next iterative in Eulerian frame.

The interaction force S_b in Eq. (6) is defined as the resultant of buoyancy, drag, virtual mass, and pressure gradient forces; it is integrated and averaged within each control volume to facilitate momentum exchange and achieve two-way Eulerian-Lagrangian coupling in the simulation, and can be expressed as

$$S_{b,i} = -\frac{1}{V_{cell,i}} \sum \left(F_{D,j} + F_{buo,j} + F_{VM,j} + F_{PG,j} \right) \tag{33}$$

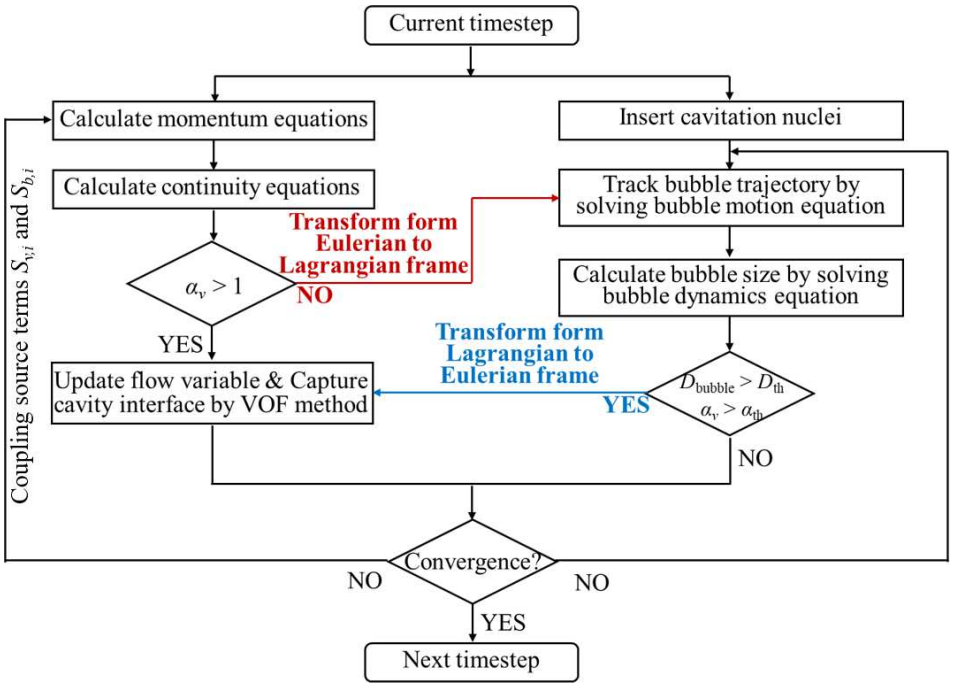


Fig.16. Computational framework of the Eulerian-Lagrangian two-way coupling algorithm.

3.5 *Configuration of critical parameters in the multiscale cavitation algorithm*

Building upon a homogeneous flow model for simulating turbulent cavitating flow in the Eulerian framework and the VOF method for capturing macroscale cavity structures, this study introduces a Discrete Bubble Model within the Lagrangian framework to track the motion and dynamic evolution of subgrid-scale discrete bubbles. This integrated approach enables effective simulation of multiscale features across various cavitating flows[33,43]. However, the accuracy of current multiscale cavitation simulations remains limited by several factors. Key quantitative parameters, such as cavitation nucleus type, number density, and average size, are often poorly characterized during the construction of the discrete bubble model. Moreover, the selection of quantitative transition thresholds in the Eulerian–Lagrangian conversion process frequently relies on arbitrary or subjective criteria. To optimize the multiscale simulation approach, the present work systematically incorporates holographic measurement data of discrete bubbles under identical cavitation conditions. By adjusting the nucleus number density and initial bubble size parameters within the stochastic nucleation process of the DBM, an appropriate bubble size threshold is established for the Eulerian–Lagrangian transition.

Previous holographic measurements of discrete bubbles have indicated that the incoming liquid flow carries a dispersion of non-condensable gas bubbles. Furthermore, in the regions where vapor structures exist, the number of discrete bubbles measured by holography sharply increases due to the formation of vapor bubbles. To capture both the entrained non-condensable bubbles and the locally generated vapor microbubbles in turbulent cavitating flow, this study employs a combined numerical strategy. This approach incorporates controlled injection of discrete bubbles upstream, along with a random nucleation method[43] applied in low-pressure zones to simulate spontaneous vapor bubble formation. As illustrated in Fig. 17, two key parameters in DBM, the bubble number density and the nucleation frequency, are derived from the experimental data. The number density of non-condensation gas bubbles carried by inflow is approximately 0.84×10^7 per cubic meter. Besides, the number density of microbubbles coming from the breakup of largescale cavities is approximately 8.56×10^7 per cubic meter, which equals the difference in the holographically measured number density of discrete bubbles between the cavitation shedding region and the freestream region. The injection frequency for both non-condensation gas bubbles and vapor bubbles in DBM depend on the incoming flow velocity and the local grid scale, which is defined as

$$f = U/\Delta l \tag{26}$$

where U is the inflow velocity and Δl is the local cell length. Meanwhile, microbubbles can rapidly reach a state of dynamic equilibrium under the influence of local pressure and velocity fields in turbulent cavitating flow. Therefore, the initial bubble diameter and distribution are considered to have negligible influence on the final morphology of discrete microbubbles in the flow field. Based on holographic measurements of microbubbles in cavitating flow, an initial microbubble diameter of 200 μm is assumed for both the inflow region and the low-pressure zone within the shedding cloud cavity, which corresponds to the time-averaged Sauter diameter of discrete bubbles within each holographic measurement range. In addition, the non-condensable gas nuclei introduced from the inflow interface, as well as the vapor bubbles arranged throughout the computational domain at each time step, are randomly initialized in their respective spaces with the defined injection frequency and a given spatial number density.

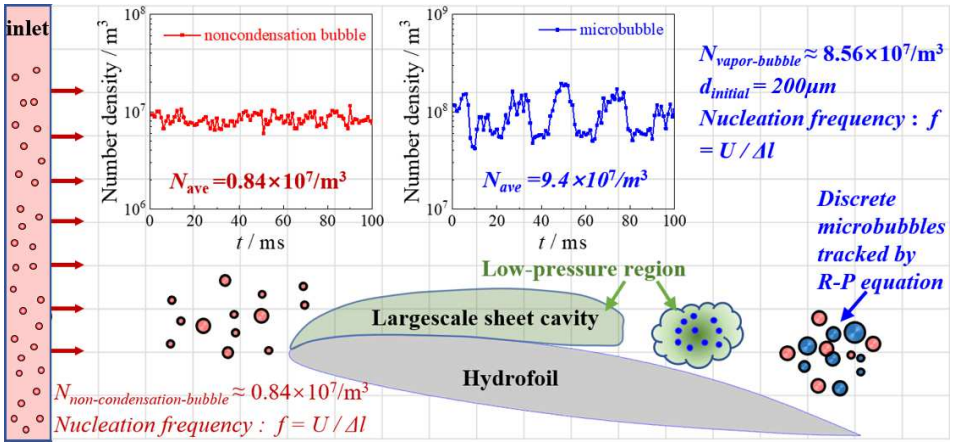


Fig.17. Schematic illustration of the modeling of non-condensable bubbles and discrete vapor bubbles in the DBM.

As another key component of the multiscale cavitation algorithm, the switching criterion between the Eulerian and Lagrangian computational strategies directly affects the accuracy of cavitation flow simulations. To address this issue, a corresponding switching mechanism is developed in this work. For the transition from the Eulerian to the Lagrangian framework, a discriminant criterion similar with existing literature on multiscale cavitation modeling is adopted[33,58,77]. when the macroscopic cavity structure becomes smaller than the local grid scale, the simulation switches to the Lagrangian framework, where the growth and motion of subgrid-scale bubbles are tracked using a discrete bubble model. Conversely, when discrete bubbles in the flow grow beyond a certain size, their morphology and dynamics can no longer be accurately described by the discrete model, and the simulation must switch back to the Eulerian framework. Specifically, based on the physical characteristics discussed in section II.C, when the critical bubble diameter exceeds 2 mm, the bubble shape notably deviates from spherical and far exceeds the scale of the local computational grid. Under such conditions, the simulation of such bubbles is switched from Lagrangian discrete tracking to the Eulerian VOF method, to more accurately capture their three-dimensional structure and interface evolution.

3.6 *Validation of multiscale cavitation model*

Fig.18. illustrates the computational domain and boundary condition setups. The numerical simulation employs a three-dimensional NACA66 hydrofoil model, with a computational domain size of $9c \times 0.3c \times 2.5c$. The center of the hydrofoil is positioned $2.25c$ from the inlet boundary and 1.25c from the top surface of the domain, which is consistent with the experimental setup. The left surface of the domain is defined as a velocity inlet, while the right surface is set as a pressure outlet. The top and bottom surfaces are specified as no-slip walls, and the front and rear surfaces are treated as symmetry planes. The outlet pressure is determined based on the cavitation number. The fluid medium is water at room temperature, with a density of 998 kg/m³ and a saturated vapor pressure of p_v = 3169 Pa. In this study, the computational domain for the numerical simulation of multiscale cavitating flow is discretized using an O-H type structured grid, with local refinement applied around the hydrofoil. To achieve an optimal balance between computational accuracy and resource consumption, a grid independence study was conducted by comparing three grid resolution strategies in our previous work [15]. The finally selected mesh strategy comprises about 4.67 million cells.

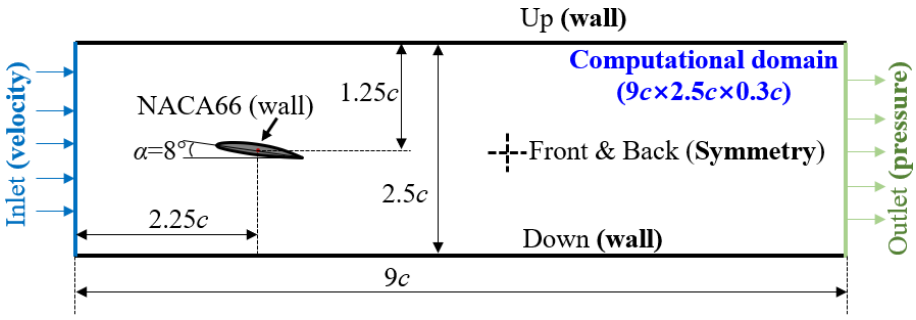


Fig.18. Setup of computational domain boundary conditions

Fig. 19 shows the frequency spectrum of the dimensionless cavity length (l / c) obtained experimentally under typical cloud cavitation conditions (σ = 1.4), compared with the pressure fluctuation spectrum at a location 0.7c from the leading edge on the suction side of the hydrofoil, as simulated by the Eulerian–Lagrangian two-way coupling numerical model established in this study. Since the transient convective evolution of cloud cavitation is the primary cause of periodic hydrodynamic fluctuations on the hydrofoil, both the dimensionless cavity length and the dominant frequency in the pressure spectrum on the suction side reflect the periodic nature of cloud cavitation. The numerical simulation yielded a dominant frequency of 46.02 Hz in the pressure fluctuations on the suction side, while the experimental result under the same condition showed a dominant frequency of 45.55 Hz in the dimensionless cavity length spectrum, with a relative error of approximately 1.03%. This corresponds to a cavitation evolution period of about 21.95 ms. Additionally, regarding the convective evolution process of cavitation, Fig. 20 presents the time-history evolution of the dimensionless cavity length over two full cycles, demonstrating good agreement between the numerical simulations and experimental measurements. The consistency in both the cloud cavitation evolution period and the macroscopic cavity length further validates the accuracy and effectiveness of the proposed Eulerian–Lagrangian two-way coupling approach in simulating the transient characteristics of cavitating flows.

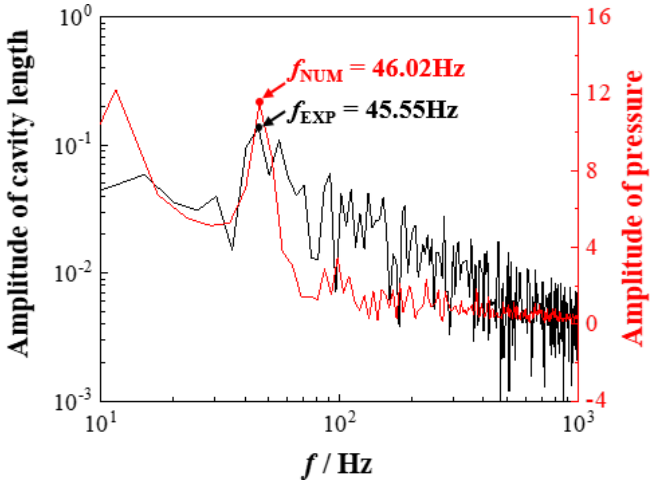


Fig.19. The frequency spectrum of fluctuation of cavity length and pressure on hydrofoil suction surface.

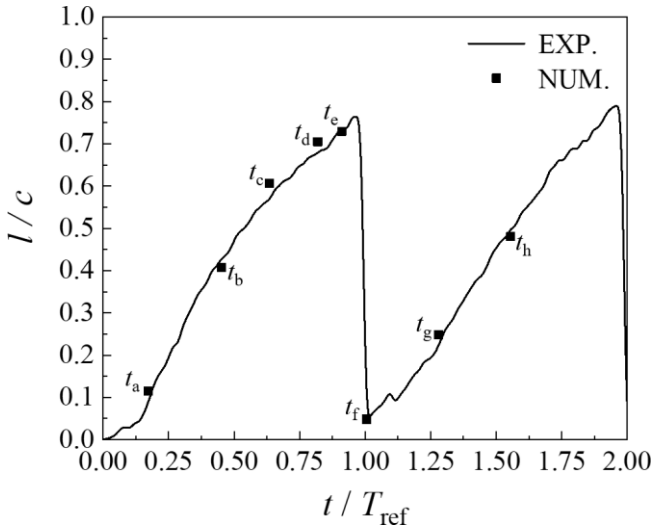
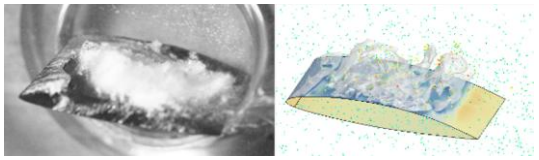
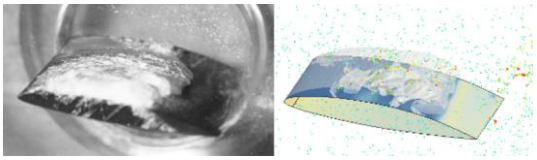


Fig.20. Comparison of experimental and numerical normalized cavity lengths (l/c) at σ = 1.4.

Fig. 21 presents a comparative visualization between the three-dimensional Eulerian–Lagrangian two-way coupling numerical simulation results and high-speed imaging experimental data of the full flow field at eight representative time instants selected from Fig. 20, in order to visually demonstrate the multi-scale cloud cavitation flow structures. During the period from t_a to t_c, the cloud cavitation is in the growth phase of the attached cavity. The attached cavity near the leading edge of the hydrofoil appears continuous and transparent, with a small number of discrete bubbles emerging near the vapor-liquid interface at the trailing edge of the attached cavity. Meanwhile, as shown in Fig. 21(c), the cloud cavity shed from the previous cycle converges into a typical U-shaped cavity structure near the trailing edge. The number and size of discrete bubbles in the region of the low-pressure vortex core are significantly larger than in other areas. From t_d to t_e, the region affected by the counter-jet exhibits intensified vapor-liquid mixing inside the attached cavity, accompanied by an increase in both the number and size of discrete bubbles. By time t_f, as the counter-jet approaches the leading edge, the reduced thickness of the macro-scale attached cavity leads to bubble breakup under disturbance, generating amount discrete microbubbles. At the instant of t_f, the shed cavity gradually aggregates into larger cloud-like vapor structures, while a new macro-scale attached sheet cavity reappears at the leading edge, as illustrated in Fig. 21(f). As the cloud-like vapor structure moves toward the wake edge of the hydrofoil, intense breakup occurs, resulting in the formation of numerous discrete bubbles, shown in Fig. 21(h). The comparative results indicate that the morphologies of the multi-scale cavitation structures around the hydrofoil observed experimentally are consistent with those obtained numerically. This agreement demonstrates that the improved Eulerian–Lagrangian two-way coupling algorithm, which incorporates cavitation nucleus content based on holographic measurements, can accurately simulate the transient evolution of multi-scale cavitating flows.



(a) t_a = 0.17 T_{ref}



(e) t_e = 0.91 T_{ref}

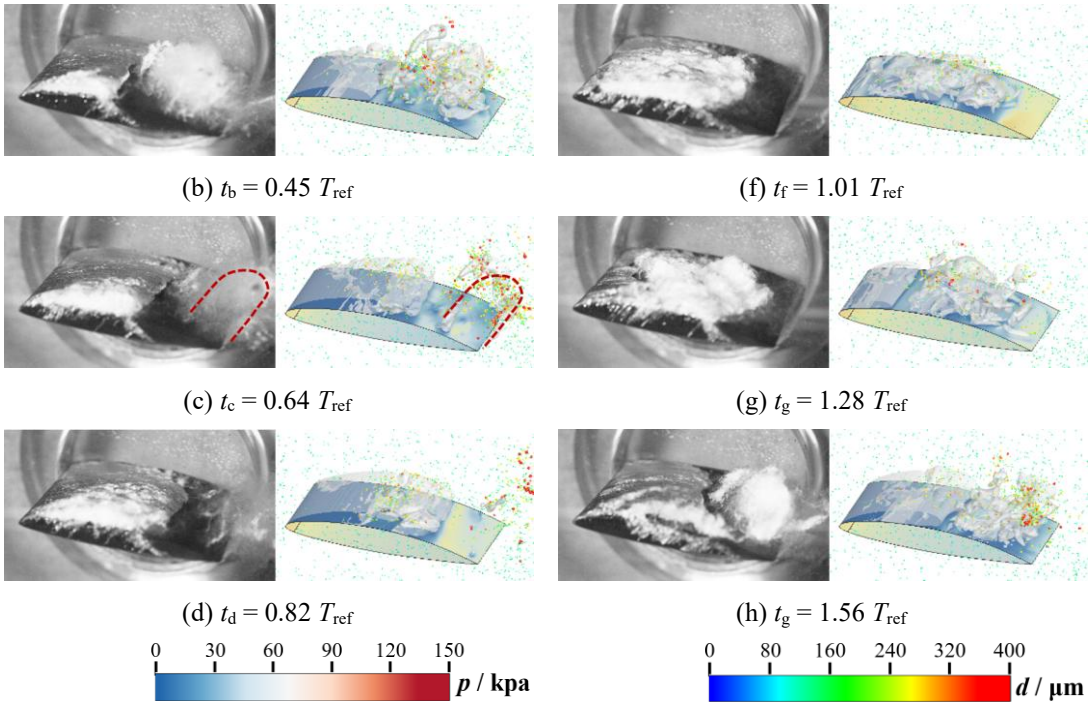


Fig.21. Comparison of oblique view results at typical moments between experimental observation and numerical prediction.

Fig. 22 provides a quantitative comparison of the transient evolution of discrete bubble number density between the numerical simulation and holographic measurement within the same flow region under multiscale cloud cavitation conditions. As shown in Fig. 22(a), in the inflow region ahead of the hydrofoil leading edge, the simulated cavitation nucleus number density agrees well with the experimental data, remaining stable over time with minor fluctuations. Fig. 22(b) demonstrates that the numerical model successfully captures the periodic fluctuations in bubble number density caused by cloud cavity shedding in the rear suction side and detachment region, showing good agreement with experimental measurements. In the wake flow region, both numerical and experimental results exhibit consistent periodic variations, with larger amplitude fluctuations compared to those in the cavity shedding region. These comparative results indicate that the improved multiscale cavitation model proposed in this study is capable of effectively representing the dynamic evolution of discrete bubbles at sub-grid scales.

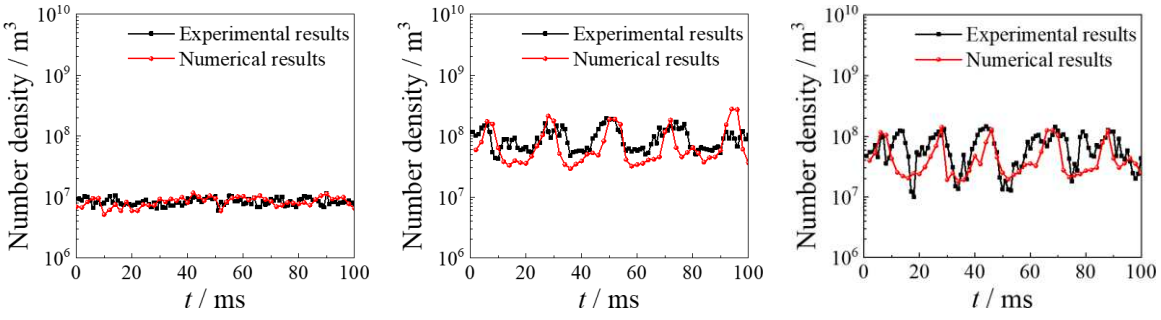


Fig.22. Comparative analysis of microbubble number density between experimental results and numerical results.

4. Conclusions

This work systematically investigates the multiscale bubble dynamics in cloud cavitating flow

around a NACA66 hydrofoil. An advanced approach for characterizing cavitating flows is developed using DIH method. Furthermore, the Eulerian–Lagrangian two-way coupled computational framework is enhanced through the incorporation of cavitation nuclei effects for improved prediction of multiscale cloud cavitation. The principal results are as follows.

(1) High-speed imaging of the full flow field reveals the unsteady convective evolution of cavitation structures. Under conditions of U = 8.5 m/s and σ = 1.4, the flow exhibits classical cloud cavitation patterns governed by the re-entrant jet mechanism. The largescale vapor cavity undergoes periodic evolution involving sequential stages of growth, re-entrant jet formation, and cloud shedding. The dominant shedding frequency is measured at 45.55 Hz, and the maximum cavity length extends to 0.8 times the chord length.

(2) Digital in-line holography (DIH) provides quantitative measurements of cavitation nuclei in the inflow, as well as the spatial and temporal distributions of large-scale vapor clusters and discrete bubbles in the cavity shedding and wake regions. Cavitation nuclei in the incoming flow remains uniformly dispersed with minimal fluctuation in number density, averaging 8.4×10^6 m^{-3}, and a Sauter mean diameter (SMD) of 191.67 μm. In contrast, the bubble number density in the cavity closure and wake regions exhibits periodic oscillations that are synchronized with the cloud cavitation evolution, peaking during the cloud cavity shedding process. The SMD of bubbles surrounding large vapor clusters is approximately 247.16 μm. Within the wake flow region, bubble collapse under high turbulence led to a progressive reduction in number density along the streamwise direction, with a time-averaged SMD of 235.63 μm. Bubble size distributions at all locations presents a dual-power-law behavior, with small bubbles following a −4/3 scaling and large bubbles a −10/3 scaling.

(3) An improved multiscale cavitation model is developed by combining a Eulerian homogeneous mixture model for continuum vapor structures and a Lagrangian discrete bubble model for mesoscale microbubbles. According to the holographic measurement results of microbubbles in the cavitation inflow region, this study determines the cavitation nuclei content and size distribution in the re-fined multiscale cavitation model. Additionally, based on the analysis of the sphericity of discrete bubbles in the cavitation region, discrete bubbles growing to 2 mm are transitioned from the Lagrangian framework to the Eulerian framework for further resolution. Meanwhile, validation against experimental data demonstrated the capability to accurately predict shedding frequency, cavity morphology, and bubble number density distributions, confirming its utility for simulating complex multiscale cavitation dynamics.

Acknowledgments

This work was supported by the Beijing Natural Science Foundation (JQ25012), and the National Natural Science Foundation of China (Grant Nos: 52441903, 92582103 and U22B6010)

Statements and Declarations

Conflict of Interest: The authors declare that they have no conflict of interest. Biao Huang is an editorial board member for the Journal of Hydrodynamics and was not involved in the editorial review, or the decision to publish this article. All authors declare that there are no other competing interests.

Author contributions: Yuntian Wang: Writing-original draft, Formal analysis, Data curation, Visualization; Beichen Tian: Conceptualization, Formal analysis, Methodology, Software, Writing-original draft; Weiye Zhong: Data curation, Software, Validation, Visualization, Formal analysis; Linmin Li: Conceptualization, Methodology, Project administration, Software, Validation; Biao Huang:

Conceptualization, Funding acquisition, Methodology, Project administration, Supervision, Writing-review & editing.

Data Availability: The data that support the findings of this study are available from the corresponding author upon reasonable request.

Ethics approval and Consent to participate: Not applicable.

References:

[1] Luo, Y., Wu, Z., Li, Z., Cheng, L., Qi, P., & Mou, J. (2025). Design of a novel pump cavitation valve and study of its cavitation characteristics. *Water*, *17*(10), 1503. https://doi.org/10.3390/w17101503

[2] Li, M. M., Hong, Y., Zhang, H. L., Wang, R. G., & He, X. D. (2025). The numerical research on cavitation performance of the composite propeller under uniform and non-uniform inflow. *Ocean Engineering*, *322*, 120399. https://doi.org/10.1016/j.oceaneng.2025.120399

[3] Praveen, S., Marimuthu, S., Alqahtani, B., Bharathiraja, G., & Gokilakrishnan, G. (2024). Enhancing bulb turbine performance assessing air injection for vibration mitigation and hydrofoil cavitation. *Journal of Applied Fluid Mechanics*, *17*(11), 2313–2332. https://doi.org/10.47176/jafm.17.11.2686

[4] Qin, X., Chen, Y., Feng, X., Shao, X., & Deng, J. (2025). A numerical investigation concerning wall-nucleation effects of the inception of sheet cavitation. *International Journal of Multiphase Flow*, *185*, 105142. https://doi.org/10.1016/j.ijmultiphaseflow.2025.105142

[5] Li, L., Pei, C., Wang, Z., Lin, Z., Li, X., & Zhu, Z. (2024). Assessment of cavitation erosion risk by eulerian–lagrangian multiscale modeling. *International Journal of Mechanical Sciences*, *262*, 108735. https://doi.org/10.1016/j.ijmecsci.2023.108735

[6] Ghahramani, E., Ström, H., & Bensow, R. E. (2021). Numerical simulation and analysis of multi-scale cavitating flows. *Journal of Fluid Mechanics*, *922*, A22. https://doi.org/10.1017/jfm.2021.424

[7] Karadağ, M. A., Göklüberk, P., & Kibar, A. (2025). Experimental and numerical investigation of flow and pressure drop in hydraulic quick connect couplings. *Flow Measurement and Instrumentation*, *106*, 102960. https://doi.org/10.1016/j.flowmeasinst.2025.102960

[8] Zhou, M., Wang, Z., Cheng, H., Ji, B., & Cao, Y. (2024). Assessment of cavitation erosion on an asymmetric hydrofoil based on energy conversion via a multiscale approach. *International Journal of Multiphase Flow*, *176*, 104820. https://doi.org/10.1016/j.ijmultiphaseflow.2024.104820

[9] Liu, Y., Wu, Q., Zhang, H., & Huang, B. (2024). Cavity dynamics and vibrations of a flexible hydrofoil in the cavitating flow. *Physical Review Fluids*, *9*, 014304. https://doi.org/10.1103/physrevfluids.9.014304

[10] Li, L., Niu, Y., Wei, G., Manickam, S., Sun, X., & Zhu, Z. (2023). Investigation of cavitation noise using eulerian-lagrangian multiscale modeling. *Ultrasonics Sonochemistry*, *97*, 106446. https://doi.org/10.1016/j.ultsonch.2023.106446

[11] Liu, H., Wang, Q., Shu, C., Hong, Y., Fang, Y., & Hao, L. (2024). Gravity-driven vertical water tunnel for modeling ventilated cavity flows around axisymmetric slender body under streamwise gravitational effect. *Acta Mechanica Sinica*, *41*(10), 324681. https://doi.org/10.1007/s10409-024-24681-x

[12] Wang, C., Wang, G., Zhang, M., Huang, B., & Ni, Y.-Q. (2023). Wall-pressure fluctuations in attached compressible turbulent cavitating flows. *Physical Review Fluids*, *8*, 114301.

https://doi.org/10.1103/physrevfluids.8.114301

[13] Chen, G., Wang, G., Hu, C., Huang, B., Gao, Y., & Zhang, M. (2015). Combined experimental and computational investigation of cavitation evolution and excited pressure fluctuation in a convergent–divergent channel. *International Journal of Multiphase Flow*, *72*, 133–140. https://doi.org/10.1016/j.ijmultiphaseflow.2015.02.007

[14] Huang, B., Young, Y. L., Wang, G., & Shyy, W. (2013). Combined experimental and computational investigation of unsteady structure of sheet/cloud cavitation. *Journal of Fluids Engineering*, *135*(7), 071301. https://doi.org/10.1115/1.4023650

[15] Tian, B., Li, L., Meng, Y., & Huang, B. (2022). Multiscale modeling of different cavitating flow patterns around NACA66 hydrofoil. *Physics of Fluids*, *34*(10), 103322. https://doi.org/10.1063/5.0117162

[16] Xu, C., & Khoo, B. C. (2020). Dynamics of the supercavitating hydrofoil with cavitator in steady flow field. *Physics of Fluids*, *32*, 123307. https://doi.org/10.1063/5.0030907

[17] Kadivar, E., Timoshevskiy, M. V., Nichik, M. Yu., el Moctar, O., Schellin, T. E., & Pervunin, K. S. (2020). Control of unsteady partial cavitation and cloud cavitation in marine engineering and hydraulic systems. *Physics of Fluids*, *32*, 052108. https://doi.org/10.1063/5.0006560

[18] Katz, J. (1984). Cavitation phenomena within regions of flow separation. *Journal of Fluid Mechanics*, *140*, 397–436. https://doi.org/10.1017/S0022112084000665

[19] Iyer, C. O., & Ceccio, S. L. (2002). The influence of developed cavitation on the flow of a turbulent shear layer. *Physics of Fluids*, *14*(10), 3414–3431. https://doi.org/10.1063/1.1501541

[20] Jiang, Y., Shao, S., & Hong, J. (2018). Experimental investigation of ventilated supercavitation with gas jet cavitator. *Physics of Fluids*, *30*(1). https://doi.org/10.1063/1.5005549

[21] Hsiao, C.-T., Chahine, G. L., & Liu, H.-L. (2000). *Scaling effect on bubble dynamics in a tip vortex flow: prediction of cavitation inception and noise*. Dynaflow Inc.

[22] Wu, Y., Liu, Y., Shao, S., & Hong, J. (2019). On the internal flow of a ventilated supercavity. *Journal of Fluid Mechanics*, *862*, 1135–1165. https://doi.org/10.1017/jfm.2018.1006

[23] Che, B., Cao, L., Chu, N., Likhachev, D., & Wu, D. (2019). Dynamic behaviors of Re-entrant jet and cavity shedding during transitional cavity oscillation on NACA0015 hydrofoil. *Journal of Fluids Engineering*, *141*(6), 061101. https://doi.org/10.1115/1.4041716

[24] Callenaere, M., Franc, J.-P., Michel, J.-M., & Riondet, M. (2001). The cavitation instability induced by the development of a re-entrant jet. *Journal of Fluid Mechanics*, *444*, 223–256. https://doi.org/10.1017/s0022112001005420

[25] Kravtsova, A. Yu., Markovich, D. M., Pervunin, K. S., Timoshevskiy, M. V., & Hanjalić, K. (2014). High-speed visualization and PIV measurements of cavitating flows around a semi-circular leading-edge flat plate and NACA0015 hydrofoil. *International Journal of Multiphase Flow*, *60*, 119–134. https://doi.org/10.1016/j.ijmultiphaseflow.2013.12.004

[26] Ganesh, H., Mäkiharju, S. A., & Ceccio, S. L. (2016). Bubbly shock propagation as a mechanism for sheet-to-cloud transition of partial cavities. *Journal of Fluid Mechanics*, *802*, 37–78. https://doi.org/10.1017/jfm.2016.425

[27] Yoon, K., Qin, S., Shao, S., & Hong, J. (2020). Internal flows of ventilated partial cavitation. *Experiments in Fluids*, *61*(4), 100–115. https://doi.org/10.1007/s00348-020-2931-y

[28] Stutz, B., & Reboud, J.-L. (2000). Measurements within unsteady cavitation. *Experiments in Fluids*, *29*(6), 545–552. https://doi.org/10.1007/s003480000122

[29] Wang, Z., Cheng, H., Bensow, R. E., & Ji, B. (2024). Numerical evaluation of the bubble dynamic

influence on the characteristics of multiscale cavitating flow in the bluff body wake. *International Journal of Multiphase Flow*, *175*, 104818. https://doi.org/10.1016/j.ijmultiphaseflow.2024.104818

[30] Konno, A., Wakabayashi, K., Yamaguchi, H., Maeda, M., Ishii, N., Soejima, S., & Kimura, K. (2002). On the mechanism of the bursting phenomena of propeller tip vortex cavitation. *Journal of Marine Science and Technology*, *6*(4), 181–192. https://doi.org/10.1007/s007730200006

[31] Yamada, T., Sato, K., Kawakita, C., & Oshima, A. (2015). Study on prediction of underwater radiated noise from propeller tip vortex cavitation. *Journal of Physics: Conference Series*, *656*, 012106. https://doi.org/10.1088/1742-6596/656/1/012106

[32] Wang, X., Song, M., Cheng, H., Ji, B., & Li, L. (2024). A multiscale euler–lagrange model for high-frequency cavitation noise prediction. *Journal of Fluids Engineering*, *146*(6), 61502. https://doi.org/10.1115/1.4064296

[33] Wang, Z., Cheng, H., & Ji, B. (2021). Euler–lagrange study of cavitating turbulent flow around a hydrofoil. *Physics of Fluids*, *33*(11), 112108. https://doi.org/10.1063/5.0070312

[34] Wan, C., Wang, B., Wang, Q., Fang, Y., Liu, H., Zhang, G., Xu, L., & Peng, X. (2017). Probing and imaging of vapor–water mixture properties inside partial/cloud cavitating flows. *Journal of Fluids Engineering*, *139*(3), 031303. https://doi.org/10.1115/1.4035013

[35] Stutz, B., & Reboud, J. L. (1997). Experiments on unsteady cavitation. *Experiments in Fluids*, *22*(3), 191–198. https://doi.org/10.1007/s003480050037

[36] Zhang, H., Liu, Y., Wang, B., & Cheng, X. (2022). Phase-resolved characteristics of bubbles in cloud cavitation shedding cycles. *Ocean Engineering*, *256*, 111529. https://doi.org/10.1016/j.oceaneng.2022.111529

[37] Liu, Y., Zhang, H., Zhang, W., & Wang, B. (2023). Bubble size distribution at early stage of hydrodynamic cloud cavitation. *Physics of Fluids*, *35*(6), 063305. https://doi.org/10.1063/5.0154309

[38] Gabor, D. (1948). A new microscopic principle. *Nature*, *161*(4098), 777–778. https://doi.org/10.1038/161777a0

[39] Coppola, G., & Ferrara, M. A. (2020). Polarization-sensitive digital holographic imaging for characterization of microscopic samples: recent advances and perspectives. *Applied Sciences*, *10*(13), 4520. https://doi.org/10.3390/app10134520

[40] Lebrun, D., Allano, D., Méès, L., Walle, F., Corbin, F., Boucheron, R., & Fréchou, D. (2011). Size measurement of bubbles in a cavitation tunnel by digital in-line holography. *Applied Optics*, *50*(34), H1. https://doi.org/10.1364/ao.50.0000h1

[41] Kato, H., Yamaguchi, H., Maeda, M., Kawanami, Y., & Nakasumi, S. (1999). Laser holographic observation of cavitation cloud on a foil section. *Journal of Visualization*, *2*(1), 37–50. https://doi.org/10.1007/BF03182550

[42] Khoo, M. T., Venning, J. A., Pearce, B. W., Takahashi, K., Mori, T., & Brandner, P. A. (2020). Natural nuclei population dynamics in cavitation tunnels. *Experiments in Fluids*, *61*(2), 34. https://doi.org/10.1007/s00348-019-2843-x

[43] Li, L., Wang, Z., Li, X., & Zhu, Z. (2021). Multiscale modeling of tip-leakage cavitating flows by a combined volume of fluid and discrete bubble model. *Physics of Fluids*, *33*(6), 062104. https://doi.org/10.1063/5.0054795

[44] Wang, C., Wang, G., & Huang, B. (2020). Dynamics of unsteady compressible cavitating flows associated with the cavity shedding. *Ocean Engineering*, *209*. (WOS:000542188700021). https://doi.org/10.1016/j.oceaneng.2020.107025

[45] Yin, T., & Pavesi, G. (2025). Several compressible computational fluid dynamics methods applied to transient sheet/cloud cavitation. *Physics of Fluids*, *37*, 023322. https://doi.org/10.1063/5.0252333

[46] Cheng, H. Y., Bai, X. R., Long, X. P., Ji, B., Peng, X. X., & Farhat, M. (2020). Large eddy simulation of the tip-leakage cavitating flow with an insight on how cavitation influences vorticity and turbulence. *Applied Mathematical Modelling*, *77*, 788–809. https://doi.org/10.1016/j.apm.2019.08.005

[47] Chen, J., Huang, B., Liu, T., Wang, Y., & Wang, G. (2021). Numerical investigation of cavitation-vortex interaction with special emphasis on the multistage shedding process. *Applied Mathematical Modelling*, *96*, 111–130. https://doi.org/10.1016/j.apm.2021.02.003

[48] Singhal, A. K., Athavale, M. M., Li, H., & Jiang, Y. (2002). Mathematical basis and validation of the full cavitation model. *Journal of Fluids Engineering*, *124*(3), 617–624. https://doi.org/10.1115/1.1486223

[49] Sussman, M. (2003). A second order coupled level set and volume-of-fluid method for computing growth and collapse of vapor bubbles. *Journal of Computational Physics*, *187*(1), 110–136. https://doi.org/10.1016/s0021-9991(03)00087-1

[50] Sussman, M. (2005). A parallelized, adaptive algorithm for multiphase flows in general geometries. *Computers and Structures*, *83*(6–7), 435–444. https://doi.org/10.1016/j.compstruc.2004.06.006

[51] Hsiao, C.-T., Ma, J., & Chahine, G. L. (2017). Multiscale tow-phase flow modeling of sheet and cloud cavitation. *International Journal of Multiphase Flow*, *90*, 102–117. https://doi.org/10.1016/j.ijmultiphaseflow.2016.12.007

[52] Maeda, K., & Colonius, T. (2018). Eulerian–lagrangian method for simulation of cloud cavitation. *Journal of Computational Physics*, *371*, 994–1017. https://doi.org/10.1016/j.jcp.2018.05.029

[53] Qin, X., Zhang, B., Li, Y., Huang, Y., Shao, X., & Deng, J. (2025). Numerical simulation of tip vortex cavitation using a multiscale method. *International Journal of Multiphase Flow*, *188*, 105183. https://doi.org/10.1016/j.ijmultiphaseflow.2025.105183

[54] Giannadakis, E., Gavaises, M., & Arcoumanis, C. (2008). Modelling of cavitation in diesel injector nozzles. *Journal of Fluid Mechanics*, *616*, 153–193. https://doi.org/10.1017/s0022112008003777

[55] Chahine, G. L. (2009). Numerical simulation of bubble flow interactions. *Journal of Hydrodynamics*, *21*(3), 316–332. https://doi.org/10.1016/S1001-6058(08)60152-3

[56] Ma, J., Hsiao, C.-T., & Chahine, G. L. (2017). A physics based multiscale modeling of cavitating flows. *Computers & Fluids*, *145*, 68–84. https://doi.org/10.1016/j.compfluid.2016.12.010

[57] Li, L., Wang, Z., Li, X., Wang, Y., & Zhu, Z. (2021). Very large eddy simulation of cavitation from inception to sheet/cloud regimes by a multiscale model. *China Ocean Engineering*, *35*(3), 361–371. https://doi.org/10.1007/s13344-021-0033-0

[58] Wang, Z. (2023). Investigation on multiscale features of cavitating flow in convergent-divergent test section using eulerian–lagrangian method. *International Journal of Mechanical Sciences*, 0–16.

[59] Tian, B., Huang, B., Li, L., & Wu, Y. (2024). Eulerian–lagrangian multiscale numerical analysis of multimodal partial shedding dynamics. *International Journal of Multiphase Flow*, *178*, 104876. https://doi.org/10.1016/j.ijmultiphaseflow.2024.104876

[60] Zhang, B., Qin, X., Chen, Y., Shao, X., & Deng, J. (2025). Numerical analysis of nucleation effects on cloud cavitation using multiscale euler–lagrange model. *Physics of Fluids*, *37*, 022103. https://doi.org/10.1063/5.0249952

[61] Tian, B., Zong, Z., Wu, Y., Huang, B., & Liu, D. (2024). Mechanism of multiscale cavitation induced pressure pulses on a propeller. *Physical Review Fluids*, *9*(11), 114302. https://doi.org/10.1103/PhysRevFluids.9.114302

[62] Zhang, Y. (2008). Measurement of geometrical parameters of microstructure with digital holography. *Infrared and Laser Engineering*.

[63] Huang, J., Weiwei Cai, Wu, Y., & Wu, X. (2022). Recent advances and applications of digital holography in multiphase reactive/nonreactive flows: a review. *Measurement Science and Technology*, *33*(2), 22001. https://doi.org/10.1088/1361-6501/ac32ea

[64] Garrett, C., Li, M., & Farmer, D. (2000). The connection between bubble size spectra and energy dissipation rates in the upper ocean. *Journal of Physical Oceanography*, *30*(9), 2163–2171. https://doi.org/10.1175/1520-0485(2000)030%3C2163:TCBBSS%3E2.0.CO;2

[65] Wang, Z., Cheng, H., Ji, B., & Peng, X. (2023). Numerical investigation of inner structure and its formation mechanism of cloud cavitating flow. *International Journal of Multiphase Flow*, *165*, 104484. https://doi.org/10.1016/j.ijmultiphaseflow.2023.104484

[66] Tian, B., Huang, B., & Li, L.. (2023). Investigation of transient sheet/cloud cavitating flow dynamics from multiscale perspective. *Physics of Fluids*, *35*(7), 77115. https://doi.org/10.1063/5.0159763

[67] Baldy, S. (1993). A generation-dispersion model of ambient and transient bubbles in the close vicinity of breaking waves. *Journal of Geophysical Research: Oceans*, *98*(C10), 18277–18293. https://doi.org/10.1029/93jc01627

[68] Hinze, J. O. (1955). Fundamentals of the hydrodynamic mechanism of splitting in dispersion processes. *AIChE Journal*, *1*(3), 289–295. https://doi.org/10.1002/aic.690010303

[69] Chan, W. H. R., Johnson, P. L., & Moin, P. (2021). The turbulent bubble break-up cascade. Part 1. Theoretical developments. *Journal of Fluid Mechanics*, *912*, A42. https://doi.org/10.1017/jfm.2020.1083

[70] Brocchini, M., & Peregrine, D. H. (2001). The dynamics of strong turbulence at free surfaces. Part 1. Description. *Journal of Fluid Mechanics*, *449*, 225–254. https://doi.org/10.1017/S0022112001006012

[71] Keller, A. (2001). *Cavitation scale effects - empirically found relations and the correlation of cavitation number and hydrodynamic coefficients*.

[72] Nicoud, F., & Ducros, F. (1999). Subgrid-scale stress modelling based on the square of the velocity gradient tensor. *Flow, Turbulence and Combustion*, *62*(3), 183–200. https://doi.org/10.1023/a:1009995426001

[73] Morsi, S. A., & Alexander, A. J. (1972). An investigation of particle trajectories in two-phase flow systems. *Journal of Fluid Mechanics*, *55*(2), 193–208. https://doi.org/10.1017/s0022112072001806

[74] Pudasaini, S. P. (2019). A fully analytical model for virtual mass force in mixture flows. *International Journal of Multiphase Flow*, *113*, 142–152. https://doi.org/10.1016/j.ijmultiphaseflow.2019.01.005

[75] Duan, H., Ren, Y., & Zhang, L. (2018). Effects of interphase forces on fluid flow in gas-stirred steel ladles using the eulerian–lagrangian multiphase approach. *JOM*, *70*(10), 2128–2138. https://doi.org/10.1007/s11837-018-3045-3

[76] Schiller, L. (1935). A drag coefficient correlation. *V.D.I. Zeitung*, *77*, 318.

[77] Peters, A., & El Moctar, O. (2020). Numerical assessment of cavitation-induced erosion using a

multi-scale euler–lagrange method. *Journal of Fluid Mechanics*, *894*, A19. https://doi.org/10.1017/jfm.2020.273